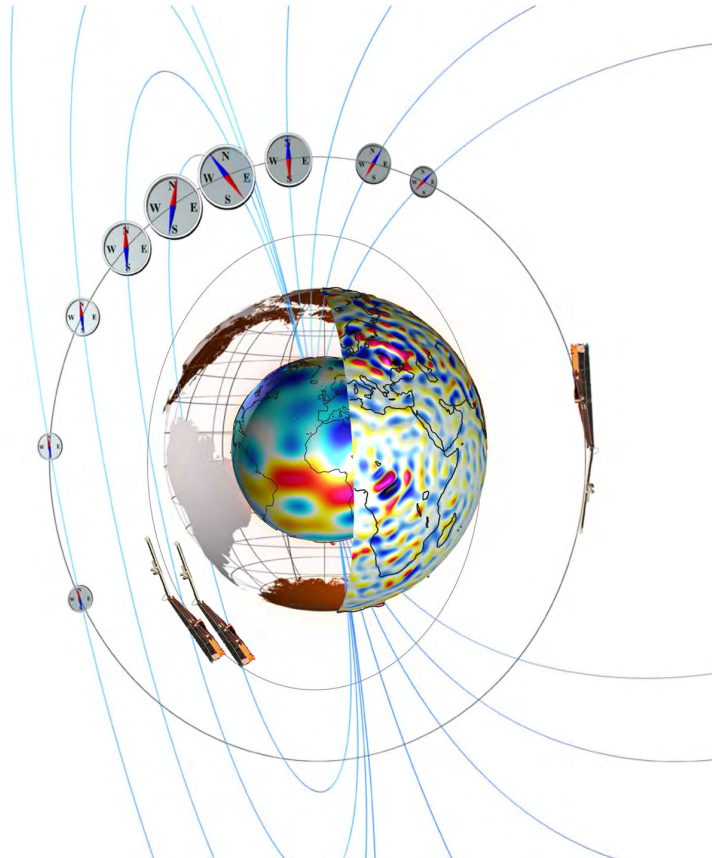

Data, Innovation, and Science Cluster

Validation of Auroral Electrojet and auroral Boundaries estimated from Swarm observations



Doc.No: SW-VR-FMI-GS-001_1-2_AEBS_VAL, Rev: 1B

Prepared:

Ari Viljanen

Ari Viljanen, Liisa Juusola, Mirjam Kellinsalmi,
Sebastian Käki
Finnish Meteorological Institute Date 20 October 2020

Prepared:

Nils Olsen

Nils Olsen
Technical University of Denmark
Chao Xiong
GeoForschungsZentrum Potsdam Date 20 October 2020

Approved:

Klaus Nielsen
Technical University of Denmark

Date

Checked:

Kirsti Kauristie

Kirsti Kauristie
Finnish Meteorological Institute

Date

© Finnish Meteorological Institute, Finland, 2020. Proprietary and intellectual rights of Finnish Meteorological Institute, Finland, are involved in the subject-matter of this material and all manufacturing, reproduction, use, disclosure, and sales rights pertaining to such subject-matter are expressly reserved. This material is submitted for a specific purpose as agreed in writing, and the recipient by accepting this material agrees that this material will not be used, copied, or reproduced in whole or in part nor its contents (or any part thereof) revealed in any manner or to any third party, except own staff, to meet the purpose for which it was submitted and subject to the terms of the written agreement.

This document is released for use only if signed by the Project Manager or the Team Leader.

Page 2 of 67

Record of changes

Reason	Description	Rev	Date
Initial version	Released	1 dA	2020-06-04
Final review	Sect. 4.2.4: updated	1 dB	2020-10-20

Table of Contents

Executive summary	5
1 Introduction	6
2 Applicable and Reference Documentation	7
2.1 Applicable documents	7
2.2 Reference documents	7
2.3 Acronyms	9
3 Background Information and Quality Assessment	10
3.1 SECS method	10
3.1.1 Baseline field	10
3.1.2 Coordinate frames and quality flags	10
3.1.3 Notes about the root-mean-square error and confidence	15
3.2 LC method	17
3.3 AOB method	17
3.3.1 AOB derived from small-scale field-aligned current (FAC) signatures	17
3.3.2 Quality flags	17
4 Validation of Products	20
4.1 Sanity checks	20
4.1.1 LC method	20
4.1.2 SECS method	20
4.1.3 AOB method	24
4.2 Validation with independent reference material	27
4.2.1 Validation of LC estimates with AMPS model values	27
4.2.2 Comparison of SECS estimates with ground-based magnetometer data	29
4.2.3 SECS estimates and equivalent currents derived from the ground magnetic field	36
4.2.4 AOB vs DMSP	41
4.2.5 Swarm AOB product vs empirical AOBFAC model	46
4.3 Cross-comparison between products	47
4.3.1 LC vs SECS	47
4.3.2 AOB vs SECS method	52
4.3.3 FAC values by SECS versus L2 FAC-dual product	52
A Appendix	57
A.1 More details about the selection of the baseline field (SECS method)	57
A.2 Statistical results (SECS method)	62
A.3 Empirical AOBFAC model vs DMSP AOB product	65
A.4 Remarks of quality flags	66

Executive summary

The study for Auroral Electrojet and auroral Boundaries estimated from Swarm observations (AEBS) aims at determining the location of auroral electrojets and auroral oval boundaries. The input data, residual magnetic field, come from three Swarm satellites (A,B,C) of which A and C fly at the same altitude and B has a higher orbit. The products are based on three modelling methods: the method of Spherical Elementary Current Systems (SECS), the Line Current (LC) method and the Auroral Oval Boundary (AOB) method.

The primary output of the SECS method consists of the divergence-free (DF) and curl-free (CF) ionospheric current densities; the CF system has an associated field-aligned current (FAC) system too. DF currents produce a magnetic field below the ionosphere whereas the field by CF currents with FAC is only observable above the ionosphere. The LC method provides only DF currents. The AOB method uses a standard Swarm data product of FAC to determine the poleward and equatorward oval boundaries. The boundaries determined by the SECS and LC methods are based on detecting the latitude bands of the strongest eastward and westward electrojets.

The methods are validated with independent reference material. For the LC method, the Average Magnetic Field and Polar Current System (AMPS) model based on CHAMP and Swarm satellites is applied. The output by the SECS method is in turn compared with the geomagnetic variation field measured by the IMAGE magnetometer network, and also with the equivalent ionospheric currents derived from IMAGE data. For the AOB method, comparison is performed with the oval boundaries available from Defense Meteorological Satellite Program (DMSP) satellites. Synthetic magnetic field generated by AMPS and processed by the LC method reproduce nicely the same main features in electrojets as visible in the model currents. Swarm-IMAGE comparisons yield high correlation values (>0.85) particularly when the contribution by telluric currents are removed from ground-based measurements. Also AOB-DMSP comparisons show relatively good results (typical correlation >0.55), when taking into account that the boundaries by these two methods come from very different data sets. Cross-comparisons between AEBS products reveal that SECS and LC are very consistent with each other about the latitude and intensity of the strongest electrojet currents (correlation coefficients >0.9), while in the width of electrojets larger discrepancies appear. The widths of westward electrojets by SECS show poor correlation with the oval widths by AOB, but when the latitudes of poleward and equatorward boundaries by the two methods are compared, somewhat higher correlation values are achieved (0.69-0.83).

Some care is needed when the AEBS results are used. First of all, all methods assume that the ionospheric currents are one-dimensional (1D), i.e. current densities depend only on the (quasi-dipole) latitude. In reality, there are always also longitudinal variations as, for example, ground magnetometer recordings show. However, electrojets are more or less 1D structures and they are generally well detected. As a guidance to users, quality indicators such as flags, root-mean-square errors and confidence values, belong to the product files.

1 Introduction

This document is the validation report for the Swarm Level 2 (L2) AEBS products for the Swarm Data, Innovation and Science Cluster (Swarm DISC) consortium in response to the requirements of [AD 3]. Swarm-AEBS includes the following products [AD 2]:

- AEJxLPL_2F – Latitude profiles of Westward Electrojet (WEJ) and Eastward Electrojet (EEJ) ionospheric sheet current densities using the Line Current (LC) method;
- AEJxLPS_2F – Latitude profiles of ionospheric sheet current and radial current densities using the Spherical Elementary Current Systems (SECS) method;
- AEJxPBL_2F – Auroral Electrojet Peaks and Boundaries using the Line Current method;
- AEJxPBS_2F – Auroral Electrojet Peaks, Boundaries and the maximum ground magnetic disturbance using the Spherical Elementary Current Systems method;
- AOBxFAC_2F – Auroral Oval Boundaries (AOB) using the Field-Aligned Current (FAC) method.

The Swarm-AEBS Product Definition document [AD 1] is available in the SVN folder: https://smart-svn.spacecenter.dk/svn/smart/SwarmDISC/DISC_Projects/ITT1_2_Swarm_AEBS/Deliverables/

Current or updated version of this document is available in the SVN folder: https://smart-svn.spacecenter.dk/svn/smart/SwarmDISC/DISC_Projects/ITT1_2_Swarm_AEBS/Deliverables/

The main content of this document is the following: We provide first background and quality information (Sect. 3). The main part (Sect. 4) explains how we have validated the products. There are various sanity checks followed by comparisons to results based on other than Swarm data. Then we compare AEBS products to each other. Appendix provides some supplementary results.

2 Applicable and Reference Documentation

2.1 Applicable documents

The following documents are applicable to the definitions within this document.

- [AD1] SW-DS-DTU-GS-003_1-2_AEBS_PDD. *Swarm-AEBS Product Definition Document*, 2019.
- [AD2] SW-DS-GFZ-GS-001_AEBS_DPA. *Swarm-AEBS Description of the Processing Algorithm*, 2019.
- [AD3] SW-OF-FMI-GS-112_1-2_AEBS_Proposal. *Proposal for Swarm DISC ITT 1.2, Swarm-AEBS – Auroral Electrojet and auroral Boundaries estimated from Swarm observations*, 2017.
- [AD4] SW-TR-GFZ-GS-008. *Swarm Level 2 FAC-dual Product Description*, 2017.

2.2 Reference documents

The following documents contain supporting and background information to be taken into account during the activities specified within this document.

- [RD1] O. Amm, H. Vanhamäki, K. Kauristie, C. Stolle, F. Christiansen, R. Haagmans, A. Masson, M.G.G.T. Taylor, R. Floberghagen, and C.P. Escoubet. A method to derive maps of ionospheric conductances, currents, and convection from the swarm multisatellite mission. *J. Geophys. Res. Space Physics*, 120, 3263-3282, doi:10.1002/2014JA020154, 2015.
- [RD2] O. Amm and A. Viljanen. Ionospheric disturbance magnetic field continuation from the ground to the ionosphere using spherical elementary current systems. *Earth Planets and Space*, 51, 431-440, doi:10.1186/BF03352247, 1999.
- [RD3] C.C. Finlay, N. Olsen, S. Kotsiaros, N. Gillet, and L. Tøffner-Clausen. Recent geomagnetic secular variation from Swarm and ground observatories as estimated in the CHAOS-6 geomagnetic field model. *Earth Planets and Space*, 68, 112, doi:10.1186/s40623-016-0486-1, 2016.
- [RD4] L. Juusola, K. Kauristie, H. Vanhamäki, A. Aikio, and M. van de Kamp. Comparison of auroral ionospheric and field-aligned currents derived from Swarm and ground magnetic field measurements. *J. Geophys. Res. Space Physics*, 121, 9256-9283, doi:10.1002/2016JA022961, 2016.
- [RD5] L.M. Kilcommons, R.J. Redmon, and D.J. Knipp. A new DMSP magnetometer and auroral boundary data set and estimates of field-aligned currents in dynamic auroral boundary coordinates. *J. Geophys. Res. Space Physics*, 122, 9068-9079, doi:10.1002/2016JA023342, 2017.
- [RD6] K.M. Laundal, C.C. Finlay, N. Olsen, and J.P. Reistad. Solar wind and seasonal influence on ionospheric currents from Swarm and CHAMP measurements. *J. Geophys. Res.*, 123(5), 4402-4429, doi:10.1029/2018ja025387, 2018.

- [RD7] H. Lühr, J. Park, J.W. Gjerloev, J. Rauberg, I. Michaelis, J.M.G. Merayo, and P. Brauer. Field-aligned currents' scale analysis performed with the Swarm constellation. *Geophys. Res. Lett.*, 42, 1-8, doi:10.1002/2014GL062453, 2015.
- [RD8] S. Maus, M. Rother, C. Stolle, W. Mai, S. Choi, H. Lühr, D. Cooke, and C. Roth. Third generation of the Potsdam Magnetic Model of the Earth (POMME). *Geochem. Geophys. Geosyst.*, 7, Q07008, doi:10.1029/2006GC001269, 2006.
- [RD9] E.I. Tanskanen, A. Viljanen, T.I. Pulkkinen, R. Pirjola, L. Häkkinen, A. Pulkkinen, and O. Amm. At substorm onset, 40 % of AL comes from underground. *J. Geophys. Res.*, 106, 13119-13134, doi: 10.1029/2000JA900135, 2001.
- [RD10] A.B. Workayehu, H. Vanhamäki, and A.T. Aikio. Field-aligned and horizontal currents in the Northern and Southern Hemispheres from the Swarm satellite. *J. Geophys. Res. Space Phys.*, 124, 7231-7246, doi:10.1029/2019JA026835, 2019.
- [RD11] C. Xiong and H. Lühr. An empirical model of the auroral oval derived from CHAMP field-aligned current signatures – Part 2. *Ann. Geophys.*, 32, 623-631, doi:10.5194/angeo-32-623-2014, 2014.
- [RD12] C. Xiong, H. Lühr, H. Wang, and M.G. Johnsen. Determining the boundaries of the auroral oval from CHAMP field aligned current signatures – Part 1. *Ann. Geophys.*, 32, 609-622, doi:10.5194/angeo-32-609-2014, 2014.
- [RD13] C. Xiong, C. Stolle, P. Alken, and J. Rauberg. Relation between large-scale ionospheric field-aligned currents and electron/ion precipitations: DMSP observations. *Earth Planets and Space*, 72, 147, doi:10.1186/s40623-020-01286-z, 2020.
- [RD14] C. Xiong, C. Stolle, H. Lühr, J. Park, B.G. Fejer, and G.N. Kervalishvili. Scale analysis of the equatorial plasma irregularities derived from Swarm constellation. *Earth Planets Space*, 68, 121, doi:10.1186/s40623-016-0502-5, 2016.

2.3 Acronyms

Acronym Description

1D	One-dimensional
AEBS	Auroral Electrojet and auroral Boundaries estimated from Swarm observations
AMPS	Average Magnetic Field and Polar Current System (model)
AOB	Auroral Oval Boundaries
CHAMP	CHAllenging Minisatellite Payload, https://www.gfz-potsdam.de/champ/
CHAOS	CHAMP, Ørsted and SAC-C model of Earth's magnetic field
DIP	Spherical frame whose pole is defined the QD pole
DISC	The Data, Innovation and Science Cluster
DMSP	Defense Meteorological Satellite Program
DTU	Danish Technical University
EEJ	Eastward Electrojet
FAC	Field-Aligned Current
FMI	Finnish Meteorological Institute
GFZ	The Helmholtz Centre Potsdam - GFZ German Research Centre for Geosciences
IMAGE	International Monitor for Auroral Geomagnetic Effects, https://space.fmi.fi/image/
IMF	Interplanetary Magnetic Field
K_p	planetary geomagnetic activity index
L2	Level 2 (satellite data)
LC	Line Current
MLT	Magnetic Local Time
POMME	POtsdam Magnetic Model of the Earth
QD	Quasi-Dipole
rmse	root-mean-square error
SECS	Spherical Elementary Current Systems
SVN	SVN Repository with server located at DTU. Presently, the following URLs apply: https://smart-svn.spacecenter.dk/svn/smart/SwarmDISC/DISC_Projects/ITT1.2_Swarm_AEBS/
Swarm	Constellation of 3 ESA satellites https://earth.esa.int/web/guest/missions/esa-operational-eo-missions/swarm
UT	Universal Time
VirES	Virtual research service for Swarm, https://vires.services/
WEJ	Westward Electrojet

3 Background Information and Quality Assessment

3.1 SECS method

3.1.1 Baseline field

The Spherical Elementary Current Systems (SECS) method uses the residual magnetic field of Swarm. It is obtained from the recorded 3-component vector field from which a baseline field is subtracted. We have used data processed in January 2020. Unless otherwise mentioned, the baseline field is the sum of the CHAOS-6 core and crustal fields (CHAOS-6-Combined in VirES) and the magnetospheric field together with its induced part in the earth (CHAOS-6-MMA-Primary and CHAOS-6-MMA-Secondary) ([RD 3]). As an exception, the POMME-9 model [RD 8] has been subtracted to obtain the residual magnetic field when Swarm results are compared to ground-based IMAGE magnetometer recordings (Sect. 4.2.2). We note that the derived quantities depend on the selected baseline models. This is discussed more in Sect. A.1.

3.1.2 Coordinate frames and quality flags

The basic output of the SECS method is expressed in the spherical DIP frame (semi-QD) whose north pole is determined by the QD system as explained in [AD 2]. Consistently to the assumed 1Dimensionality, the derived ionospheric current densities depend only on the DIP latitude. We consider first the divergence-free ionospheric sheet current density (\mathbf{J}_{df}) that has only an eastward component in the DIP frame. It is the quantity used for determining electrojets. For the precise definition of the model parameters and detection of electrojets, see [AD 2]. Unless we mention otherwise, we use only oval crossings with the best quality flag (all zeros, cf. Table 1).

Before showing results, we demonstrate the difference between the QD and DIP coordinate frames a little more (Figs. 1-2). The QD coordinates and the corresponding geocentric coordinates are based on mapping along geomagnetic field lines from Swarm to the ionospheric altitude. When applying the SECS method, we used the spherical DIP frame in which the latitudes and longitudes differ from those of the QD frame. It must be noted that the north, east and downward directions in the DIP frame are not precisely equal to those in the QD frame, since the latter is not an orthogonal neither a spherical system. However, the difference is obviously small and we have not tried to convert vectors from DIP to QD. The possible error that this may cause is insignificant compared to the inaccuracy due to the 1D assumption.

Examples of the current density profiles and determination of electrojets are shown in Fig. 3. For the quality flags used in the plots, see Table 1. In all plots, the latitude axis covers the range -85 .. -50 deg or 50 .. 85 deg in the QD system. This is the latitude range where SECS method is applicable [RD 1]. As will be seen, the orbits do not always cover the full range, because the most poleward parts are not always reached. In its orbit, Swarm flies close to the geographic poles, so the orbit can be far from the QD pole.

The upper left corner represents a very clean case: the eastward and westward currents are located inside the expected oval region. There are two distinct westward electrojet sections of which the poleward one has a larger total current and is defined to represent the main westward electrojet. In the corresponding way, the main eastward electrojet can be easily found. The maximum of the modelled horizontal ground magnetic field transverse to the electrojet occurs very close to the location of the maximum eastward current density. Similarly, the minimum of the ground field is seen close to the strongest westward current density.

The upper right corner shows another case with well-defined electrojets. The eastward electrojet has a clear maximum at about -63 deg. Another region of eastward currents appears in the poleward

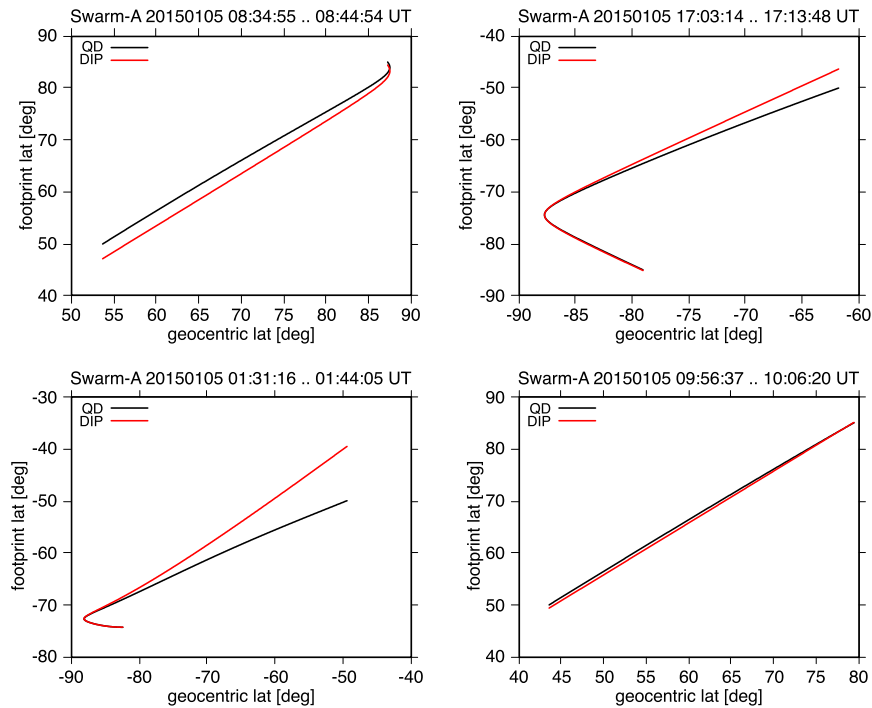


Figure 1: Examples of the QD and DIP latitudes of ionospheric footprints during oval crossings versus the corresponding geocentric latitudes.

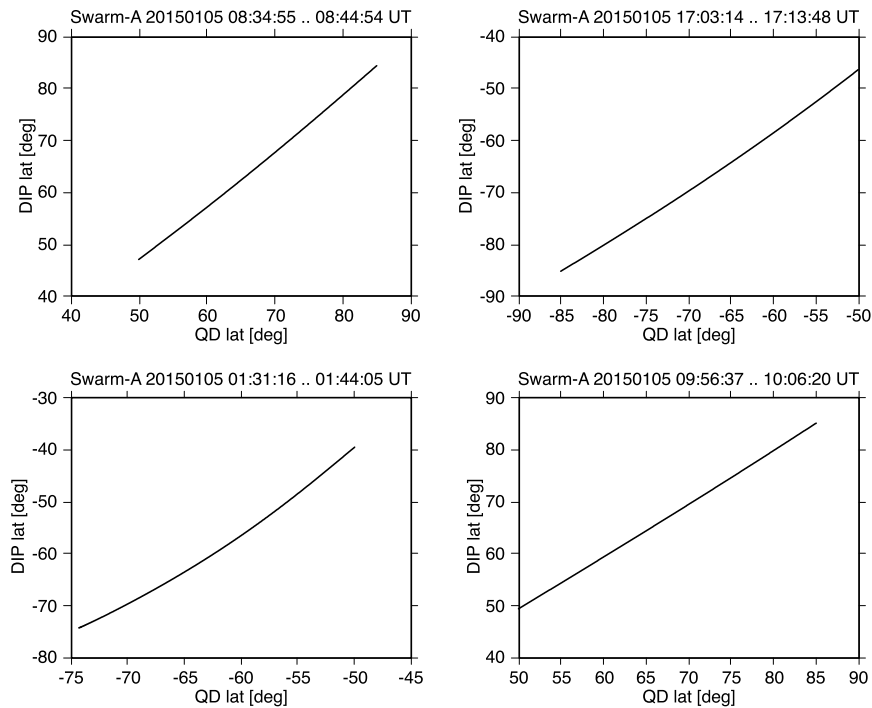


Figure 2: As Fig. 1 but DIP latitudes plotted versus QD latitudes.

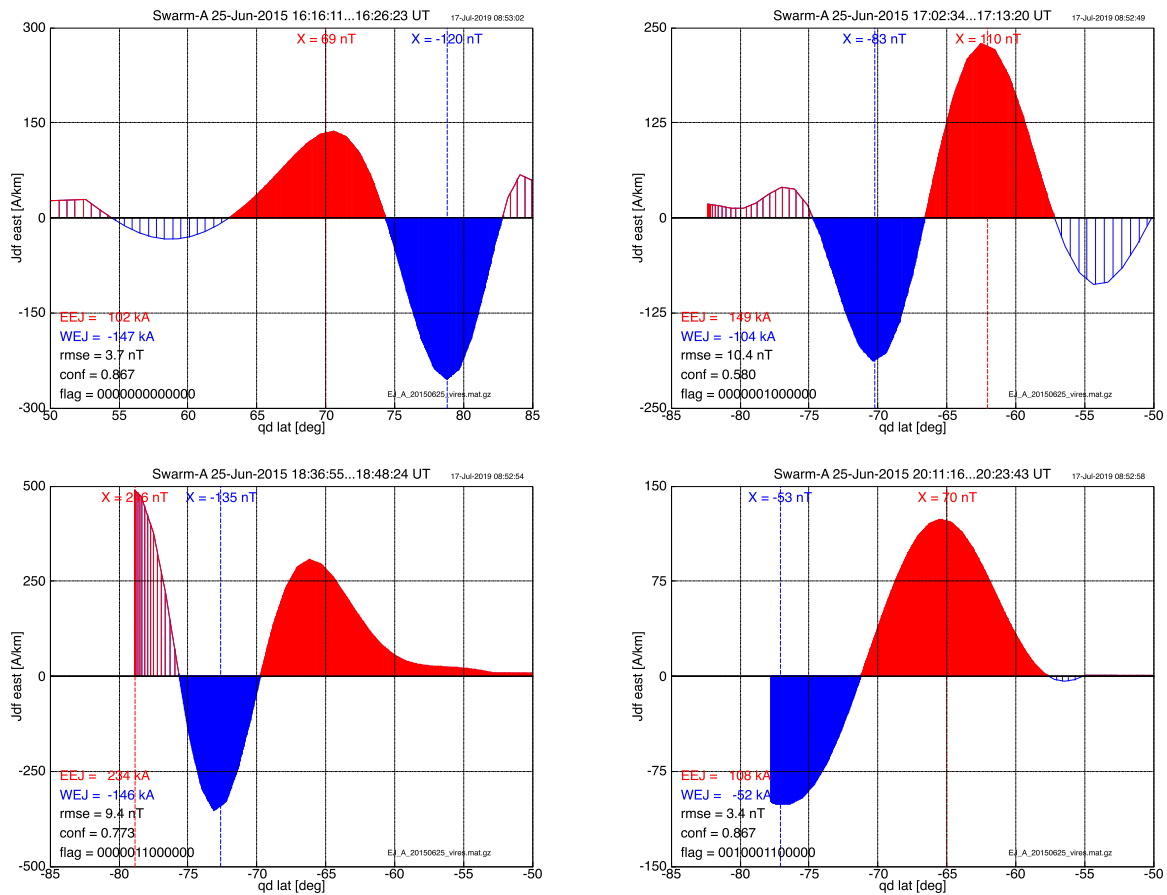


Figure 3: Examples of the divergence-free ionospheric current densities during oval crossings (Swarm-A 25 June 2015). For explanation of the flags, see Table 1. Red hatching denotes eastward current and blue denotes westward current. Uniform colouring indicates the region where the total amplitude of the electrojet is largest. Vertical coloured lines indicate the location of the minimum (blue) and maximum (red) of the modelled horizontal ground magnetic field transverse to the electrojet. Quality flags are explained in Table 1. The root-mean-square error (rmse) between the measured and fitted field-aligned component and the confidence value (conf) are also shown.

part of the oval, where the satellite orbit lacks about 2.5 degrees in latitude from the poleward boundary of the analysis area. However, the poleward section of eastward currents is obviously weak. The westward electrojet has two sections of which the poleward clearly represents the main electrojet.

In the lower left corner, the eastward electrojet is nominally well-defined. However, the most poleward region remains uncovered and some uncertainty remains whether the main eastward current would actually flow there. The maximum of the modelled ground horizontal field occurs in the poleward section, instead of being close to the centre of the nominal eastward current. In turn, the westward electrojet is well-determined. The lower right corner shows a case of a well-defined eastward electrojet, whereas the satellite orbit does not sufficiently cover the poleward area where the westward electrojet very obviously flows.

The base quality flags introduced in Table 1 describe how reliably the boundaries and peak locations of the electrojets can be detected. Due to the binary notation, there are theoretically

Table 1: Base quality flags for determination of electrojets, used both for LC and SECS products ([AD 1]).

000000000000	Both EEJ and WEJ are detected, and their current densities are zero at all boundaries.
000000000001	No eastward currents detected.
000000000010	No westward currents detected.
000000000100	Equatorward EEJ boundary occurs at the edge of the analysis area, and the density is larger than 20% of peak value.
000000001000	Poleward EEJ boundary occurs at the edge of the analysis area, and the density is larger than 20% of peak value.
000000010000	Equatorward WEJ boundary occurs at the edge of the analysis area, and the density is larger than 20% of peak value.
000000100000	Poleward WEJ boundary occurs at the edge of the analysis area, and the density is larger than 20% of peak value.
000001000000	Swarm orbit does not fully cover the predefined oval latitude range. Latitude gap is 2 degrees or larger.
000010000000	Equatorward EEJ boundary occurs at the edge of the analysis area.
000100000000	Poleward EEJ boundary occurs at the edge of the analysis area.
000100000000	Equatorward WEJ boundary occurs at the edge of the analysis area.
001000000000	Poleward WEJ boundary occurs at the edge of the analysis area.
010000000000	Peak value of EEJ occurs at the edge of the analysis area.
100000000000	Peak value of WEJ occurs at the edge of the analysis area.

$2^{13} = 8192$ different flag combinations. However, only a small number appears in practice as will be seen later. In the most ideal case (000000000000), both eastward and westward currents occur during an oval crossing and have well-defined boundaries. Fully usable are also the cases in which the current flows only eastward or westward across the whole region, and has well-defined boundaries (000000000001, 000000000010). However, there are some exceptional cases with nominally high quality, but in reality without a proper electrojet as demonstrated by comparison to ground-based data (Sect. 4.2.2).

We also note that we always use the term electrojet without trying to check whether it is consistent with the conventional definition. For example, the westward electrojet is normally associated to night-time currents occurring often with visible auroras. Our method finds westward electrojets at any time of the day. Since the Magnetic Local Time (MLT) is given in the final product files, the user can limit the time window to exclude unwanted cases.

An example of all components of the modelled current densities is shown in Fig. 4. In the region of the westward electrojet (divergence-free currents, J_{df}), there is also a southward ionospheric current (curl-free currents, J_{cf}). At the equatorward WEJ boundary, there are upward currents (radial currents, j_r), and at the poleward WEJ boundary, there are downward currents. Note that that the quality flags given in Table 1 are determined on the basis of J_{df} only.

Finally, we note that although the same definition of the quality flags is applied both in the LC and SECS methods, their occurrence differs between these methods. This is briefly discussed in Appendix A.4.

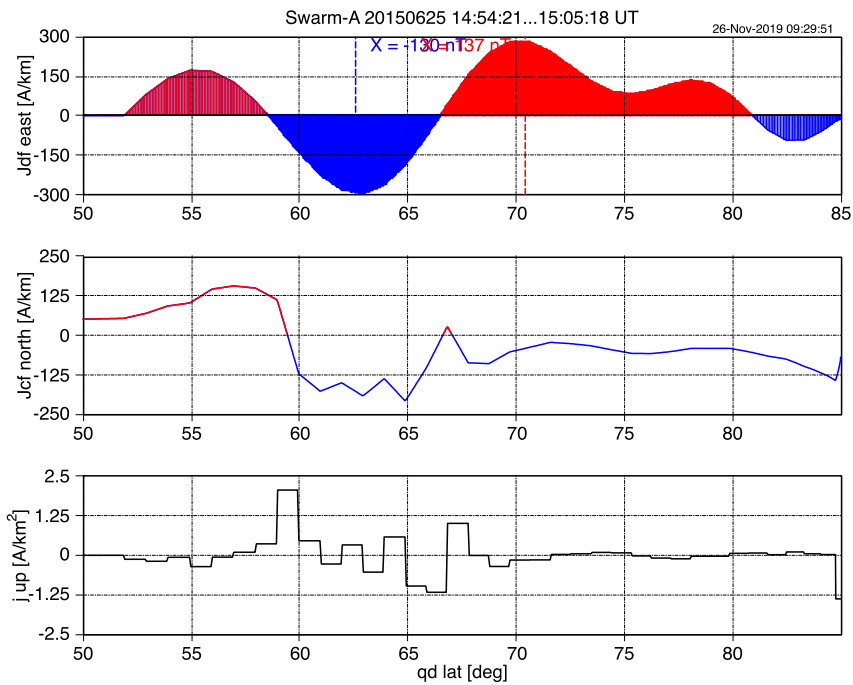


Figure 4: Example of the divergence-free (top) and curl-free (middle) ionospheric current densities and radial current density (bottom) during an oval crossing. The explanation of the colours used for the divergence-free current density is given in Fig. 3. For the curl-free current density, red refers to a northward current and blue to a southward current.

3.1.3 Notes about the root-mean-square error and confidence

The determination of the ionospheric current densities is based on the fit of the residual magnetic field component ($\delta B_{||}$) parallel to the field line [AD 2]. In practice, we consider the field in the DIP frame and define the field line direction by using the r and θ components of the baseline field. Two measures are used to characterise the success of the fit. The root-mean-square error is defined by

$$\text{rmse} = \sqrt{\langle (\delta B_{obs,||} - \delta B_{mod,||})^2 \rangle} \quad (1)$$

where $\delta B_{obs,||}$ is the observed residual field and $\delta B_{mode,||}$ is the modelled value, and $\langle .. \rangle$ refers to the mean value. The confidence value is defined by

$$\text{conf} = 1 - \frac{\text{rmse}}{\sqrt{\langle B_{obs,||}^2 \rangle}} \quad (2)$$

In the ideal case, confidence would be equal to unity.

Figure 5 shows a few examples of the fitted magnetic field. Generally, confidence values larger than about 0.90 seem to indicate a good fit such as presented in the upper row in the figure. On the other hand, there are often rapid spatial variations in the field due to field-aligned currents across which Swarm directly flies (lower row). It is not possible to reproduce them very precisely, although smoother large-scale features can still be modelled.

In the case of the SECS method, we considered also the ϕ component of the field in the DIP frame. In most cases, it gives a smaller confidence value. This is mostly due to local field-aligned currents that cause perturbations in both directions perpendicular to the local main field [RD 4].

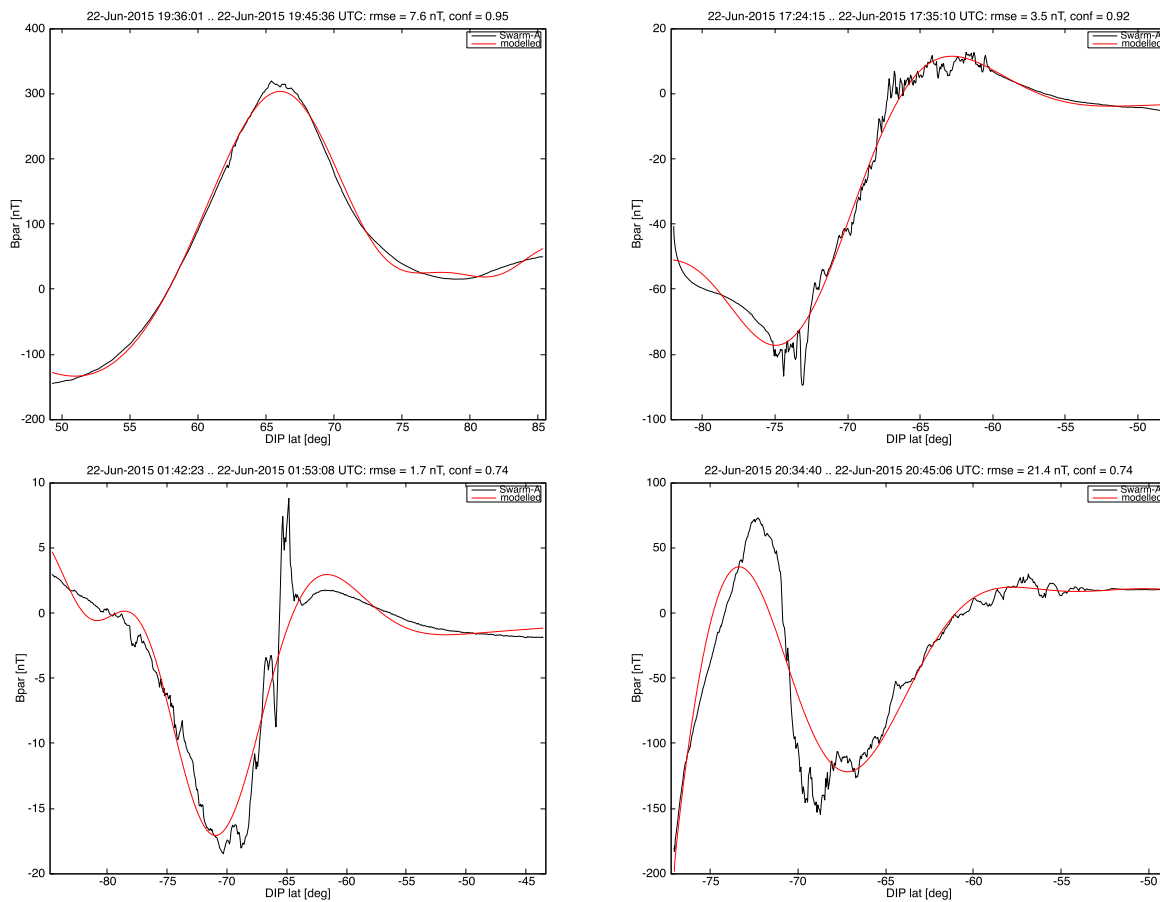


Figure 5: Measured (black) and fitted (red) magnetic field parallel to the field line defined by the r and θ components in the DIP frame.

3.2 LC method

For the LC method, background documentation is covered by [AD 2]. The same quality flags are applied as for the SECS method (Table 1).

3.3 AOB method

3.3.1 AOB derived from small-scale field-aligned current (FAC) signatures

The Auroral Oval Boundary (AOB) method is based on the small-scale (up to 10 km) FAC signatures derived from the Swarm satellites. Larger scale FAC signatures are suppressed by subtracting 20 s averaged values, corresponding approximately to 150 km along the Swarm orbits, as the auroral boundaries are more sharply detected from the small-scale FACs. The estimates of FACs (single satellite method) are routinely derived from the magnetic measurements of each Swarm spacecraft and provided as the L2 data product FACxTMS_2F. More details about determining auroral boundaries from FAC signatures can be found in [RD 11].

The outputs of the AOB product are epoch and location (in geographic and magnetic coordinates) of the equatorward and poleward boundaries for each Swarm orbital crossing of the auroral latitudes. A boundary flag, with values of 1 or 2, is used for indicating the detected boundary being equatorward or poleward, respectively. However, the equatorward and poleward boundaries are not always detected as one pair for the same auroral crossing of Swarm, which can be due to data gap or the Swarm orbit does not reach the poleward boundary of the auroral oval (mostly happens at the southern hemisphere). Therefore, a pair indicator is used for the AOB product for specifying if the auroral oval boundaries are detected as one pair, with values -1 and 1 meaning the paired boundary is in the previous or next record, respectively. If there is no paired boundary for the same oval crossing, the pair indicator is set to 0.

Figure 6 presents the magnetic local time (MLT) distribution of the detected equatorward (EAOB) and poleward (PAOB) boundaries for three Swarm satellites, respectively. The data period considered here is from December 2013 to September 2018. Overall, during nearly 5-year period, for all three Swarm satellites, there are about 4000 equatorward and 3000 poleward boundaries that are detected for each MLT bin, which account to about 97% and 70% for the whole Swarm orbits. The Swarm orbit does not always reach the magnetic pole or does not come close to it in order to cover the auroral oval poleward boundary that can explain the relatively lower number for the poleward boundaries.

3.3.2 Quality flags

In the AOB product, the boundaries are determined by finding the regions with strong FAC signatures. In this approach, two parameters, σ and P_a , are used to define the quality of the detection. σ is the standard deviation of the linear fit of FAC's intensity, the so-called S value (see details in [RD 11]), and users are suggested to use boundaries with σ less than 0.4. P_a is the linear fit of the S values, and users are suggested to use detected boundaries with P_a larger than 0.2.

Figure 7 shows the occurrence of detected boundaries over (left) σ and (right) P_a values in the northern hemisphere. Data considered are from December 2013 to September 2019. As the results from three Swarm satellites are similar, they are combined.

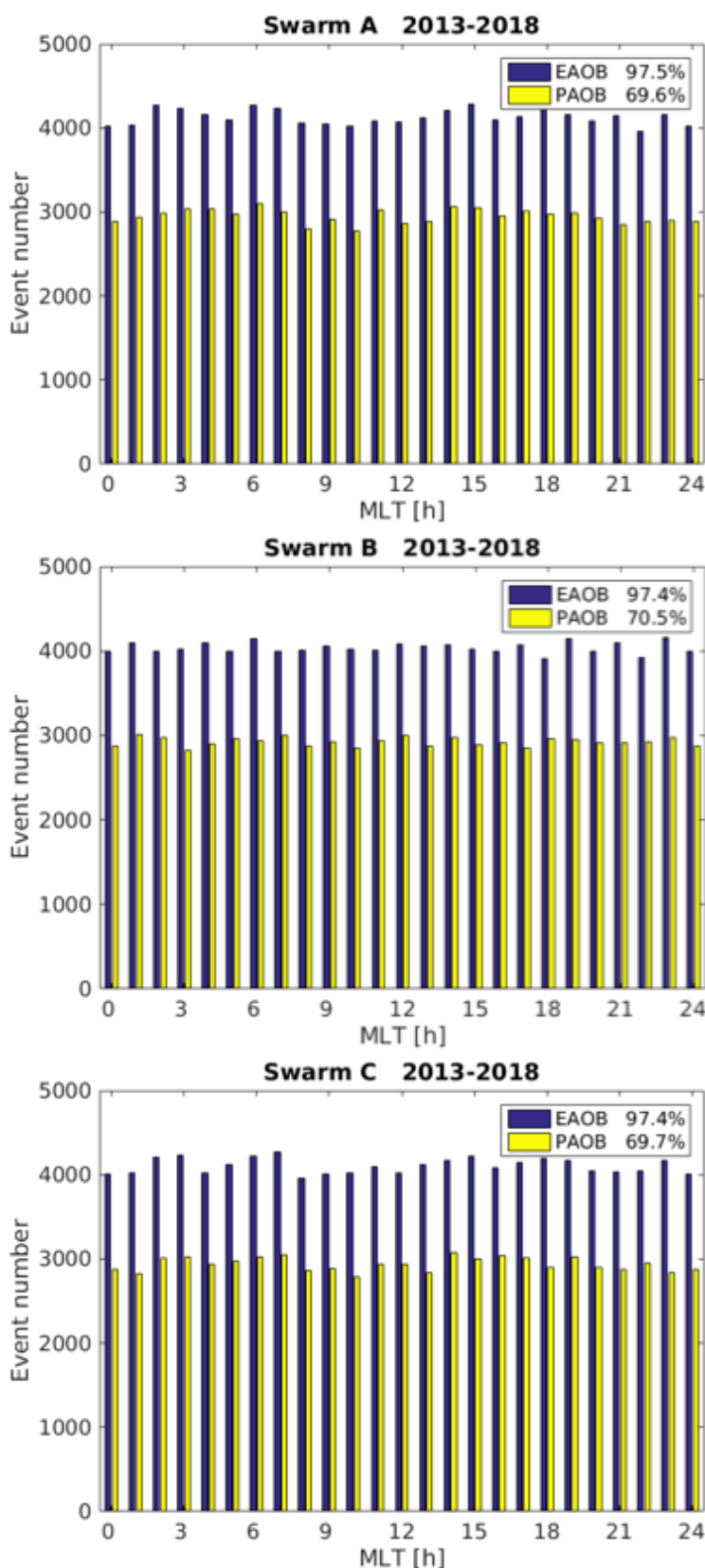


Figure 6: Magnetic local time distribution of the detected equatorward (EAOB) and poleward (PAOB) boundaries for the three Swarm satellites.

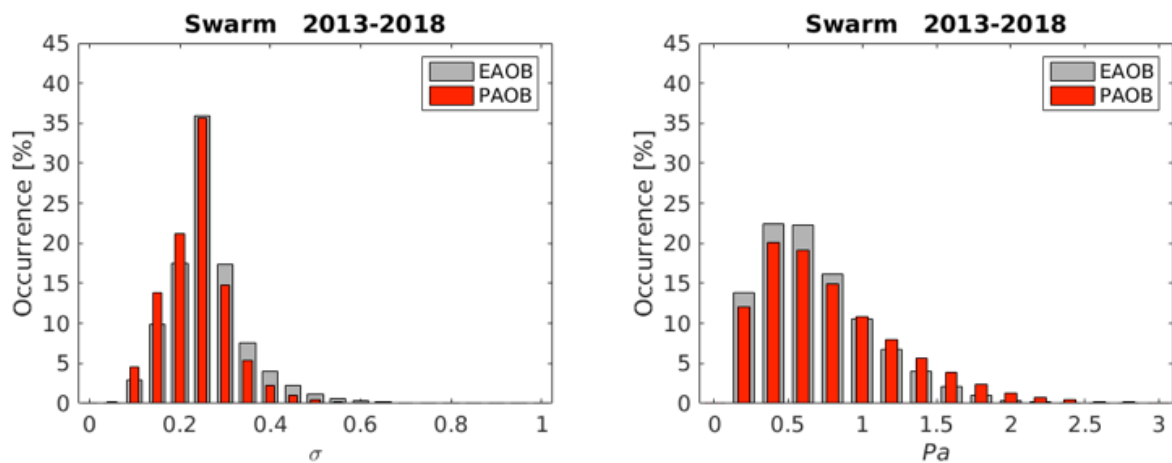


Figure 7: The occurrence of detected boundaries for the distribution on (left) σ and (right) P_a values.

4 Validation of Products

We will validate the products in three steps:

- 1) Sanity checks by a mutual comparison of the three satellites.
- 2) Comparison with independent reference material including ground-based and satellite data.
- 3) Cross-comparison between products.

4.1 Sanity checks

The Swarm satellites (A,B,C) are equipped with identical instruments. Swarm-A and Swarm-C fly at the same altitude close to each other, so they should provide nearly identical products all the time. Due to the higher altitude and different local time, the products by Swarm-B are generally different from A and C, but long-term statistics should be nearly equal by all satellites.

4.1.1 LC method

A validation of the data product LPL providing profiles of ionospheric sheet current density as derived using the Line Current (LC) method is performed by comparison with model values as given by the AMPS (Average Magnetic Field and Polar Current System) model of [RD 6] (see Sect. 4.3) and by comparison with the corresponding results obtained using the SECS method (see Sect. 4.3.1.)

4.1.2 SECS method

Swarm-A and Swarm-C have orbits at the same height (with an initial altitude of 460 km) their longitudinal separation in our validation data set is typically ~ 1.4 deg corresponding to the distance less than 170 km. So they usually cross the auroral oval nearly simultaneously and it is meaningful to compare them for each individual crossing. As the test period, we use June 2015 during which events of high activity occurred. We considered oval crossings whose mean time for both spacecraft differed at most one minute. As an additional check, we required that the footprints of the satellites must differ less than 0.5 deg in latitude and 3.0 deg in longitude during the oval crossing. Figure 8 shows the modelled amplitudes of the eastward and westward ionospheric currents. Agreement between the spacecraft is nearly perfect. Results are nearly as good for the width of the current (Fig. 9) and for the latitude at which the maximum current density occurs (Fig. 10). In Fig. 10, there is somewhat more scatter in points collected from the southern hemisphere, but the overall agreement between Swarm-A and Swarm-C is good there, as well. We repeated similar comparisons for the full year of 2018 and obtained equally good results then too (plots not shown here). This indicates that the magnetometers onboard Swarm-A and Swarm-C have remained stable.

Since Swarm-B flies at a higher altitude (initially 530 km) than the other spacecraft, it has crossed the auroral oval at the same time as them only in the beginning of the Swarm mission. For simultaneous crossings, we applied the same conditions as above for Swarm-A and Swarm-C. Figure 11 compares the maximum locations of currents between Swarm-A and Swarm-B in January 2014. Apart from a few outliers, this shows again an excellent correspondence. The same holds true for other comparisons similar to Figs. 8-9 (plots not shown here). For the later phases of the mission, we cannot any more compare Swarm-B to other satellites for simultaneous oval crossings. However, comparison of statistical results of all the three satellites indicates that the magnetic field measurements of Swarm-B have continued without problems too.

For the curl-free currents (horizontal J_{cf} , radial j_r), Fig. 12 shows comparison between Swarm-A and Swarm-C. There is again a very good correspondence.

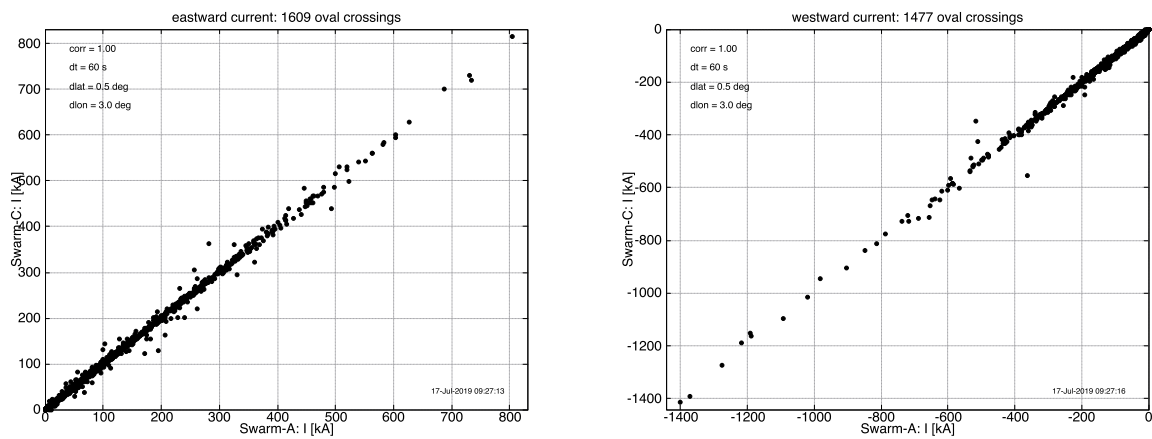


Figure 8: Amplitude of ionospheric currents modelled from Swarm-A and Swarm-C (Jun 2015). Left: eastward currents, right: westward currents. The allowed latitudinal and longitudinal difference between the ionospheric footprints is expressed by dlat and dlon.

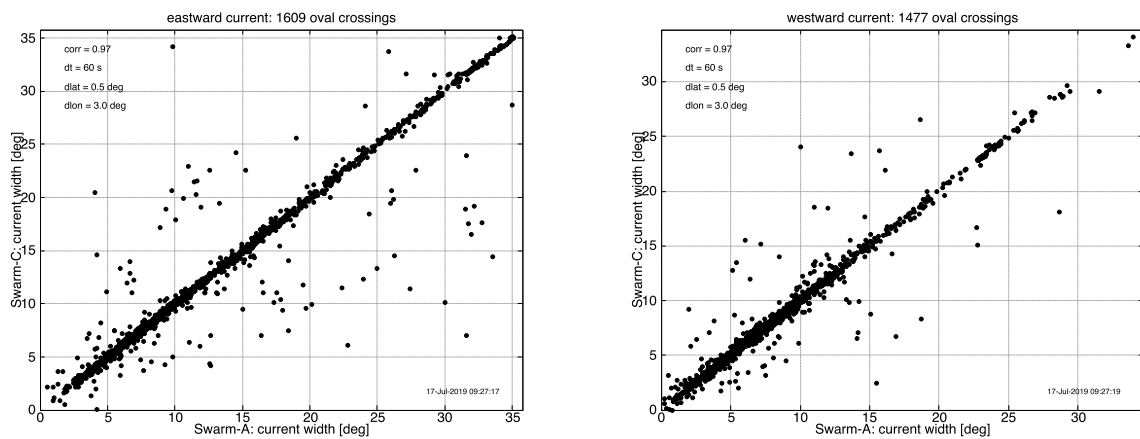


Figure 9: Width of ionospheric currents modelled from Swarm-A and Swarm-C (Jun 2015). Left: eastward currents, right: westward currents.

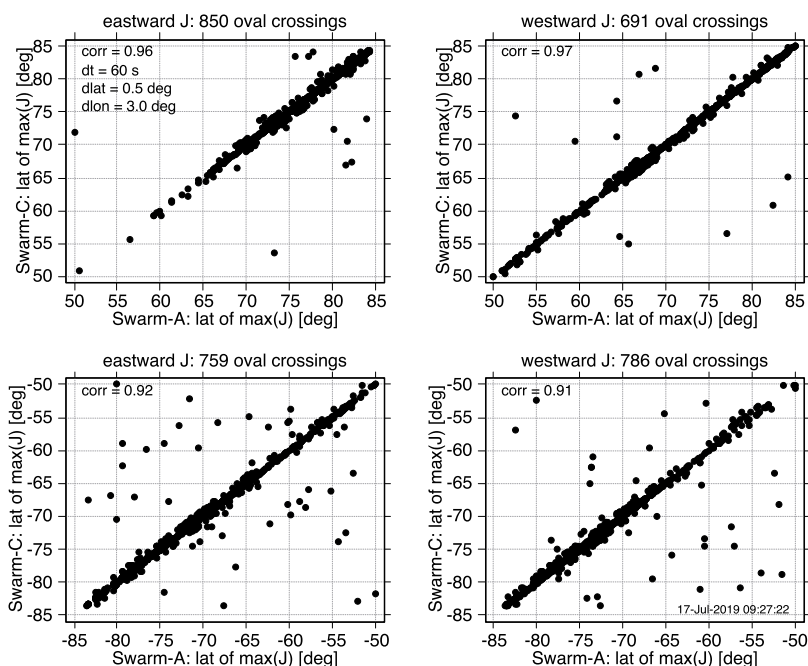


Figure 10: Location of the maximum ionospheric current density modelled from Swarm-A and Swarm-C (Jun 2015). Upper row: eastward and westward currents in the northern hemisphere. Lower row: eastward and westward currents in the southern hemisphere. The latitude is given in the QD frame as explained in [AD 2]. The allowed latitudinal and longitudinal difference between the ionospheric footprints is expressed by dlat and dlon in the upper left plot.

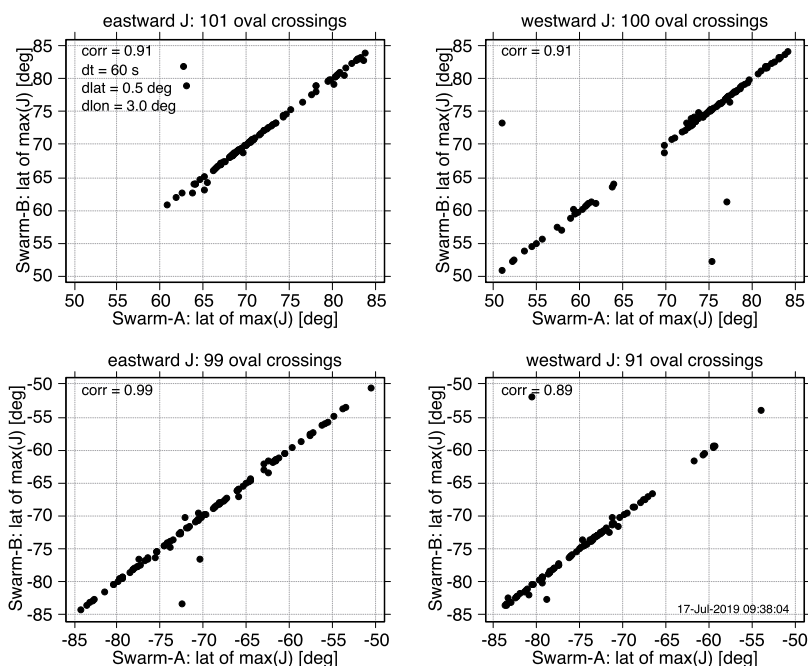


Figure 11: Location of the maximum ionospheric current density modelled from Swarm-A and Swarm-B (Jan 2014). Upper row: eastward and westward currents in the northern hemisphere. Lower row: eastward and westward currents in the southern hemisphere. The latitude is given in the QD frame as explained in [AD 2].

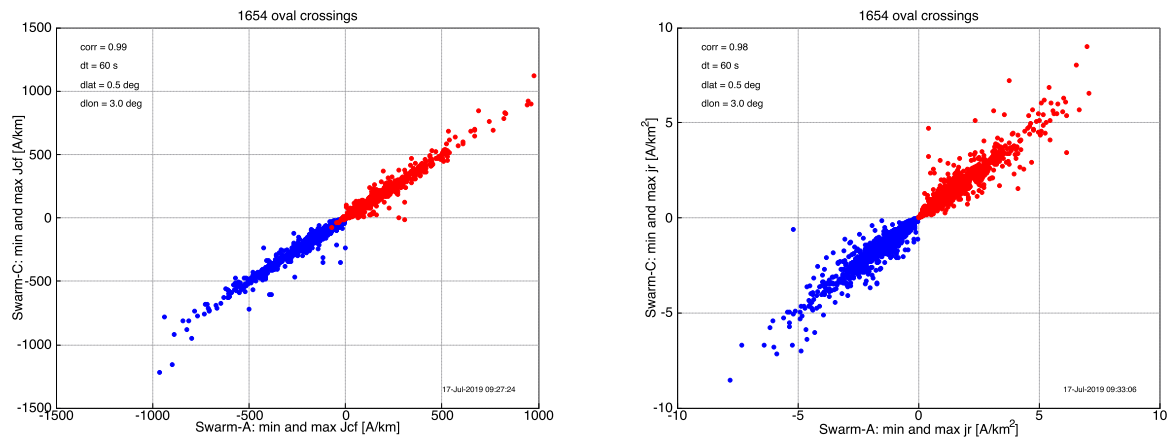


Figure 12: Left: Minimum (blue) and maximum (red) curl-free ionospheric current density modelled from Swarm-A and Swarm-C (Jun 2015). Right: Minimum (blue) and maximum (red) radial current density. The allowed latitudinal and longitudinal difference between the ionospheric footprints is expressed by dlat and dlon.

Some additional statistical results are shown in Sect. A.2.

4.1.3 AOB method

The location of the auroral ovals were determined by the auroral oval boundary (AOB) method based on modelled field-aligned currents [RD 11, 12]. For the validation of the AOB product, we provide here comparisons between the three Swarm satellites. Comparison between Swarm and DMSP satellites is presented in Sect. 4.3.

During the early mission period from Dec 2013 to Jan 2014, the three Swarm satellites were flying in a string a pearls. For this time span, we can directly compare the auroral boundaries derived from Swarm-A with the values from Swarm-B that has a higher altitude (Fig. 13). The corresponding comparison between Swarm-A and Swarm-C is shown in Fig. 14.

During the period of the final constellation (after 17 Apr 2014), Swarm-A and Swarm-C are flying side-by-side with longitudinal separation of 1.4 deg. Auroral oval boundaries derived from these data are shown in Fig. 15.

As shown in Figs. 13-15, during both mission periods, the AOB products show high consistency between the Swarm satellites. Comparing to the final constellation, the AOB products at earlier mission period have relatively larger root-mean-square (rms) level between the Swarm satellites. One possible reason for this could be that the small-scale FACs have a persistent period of the order of 10 s ([RD 7]), but the time differences between the Swarm satellites when they were flying over the same latitude gradually increase and reach as large values as 300 s at the end of Jan 2014. On the other hand, for the final constellation period, the time difference between Swarm-A and Swarm-C when they are flying over the same latitude has been confined to around 6 s (see Fig. 1 of [RD 14]).

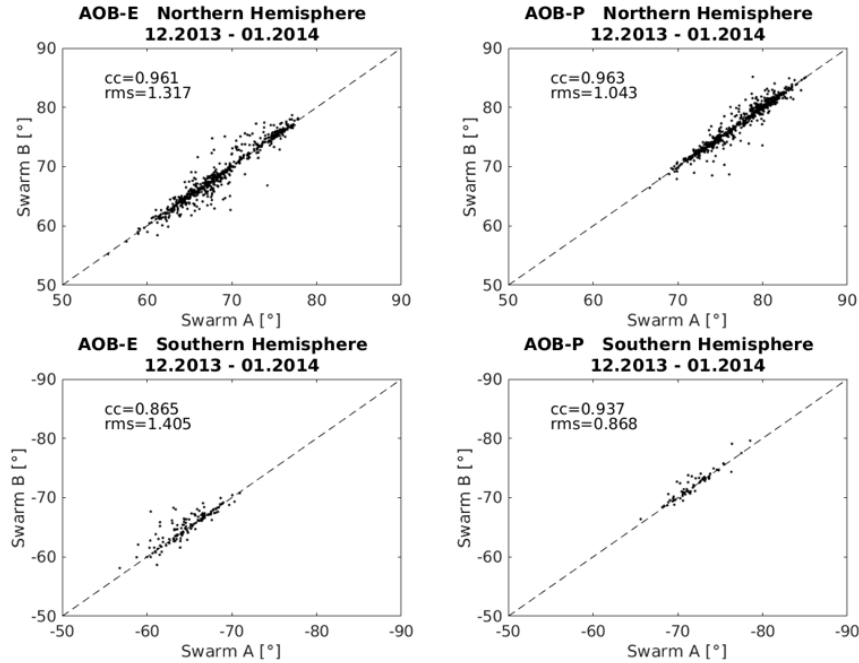


Figure 13: The (left) equatorward and (right) poleward auroral boundaries derived from Swarm-A and Swarm-B in the (top) northern and (bottom) southern hemispheres, respectively. The correlation coefficient (cc) and the root-mean-square difference (rms) are shown in each panel.

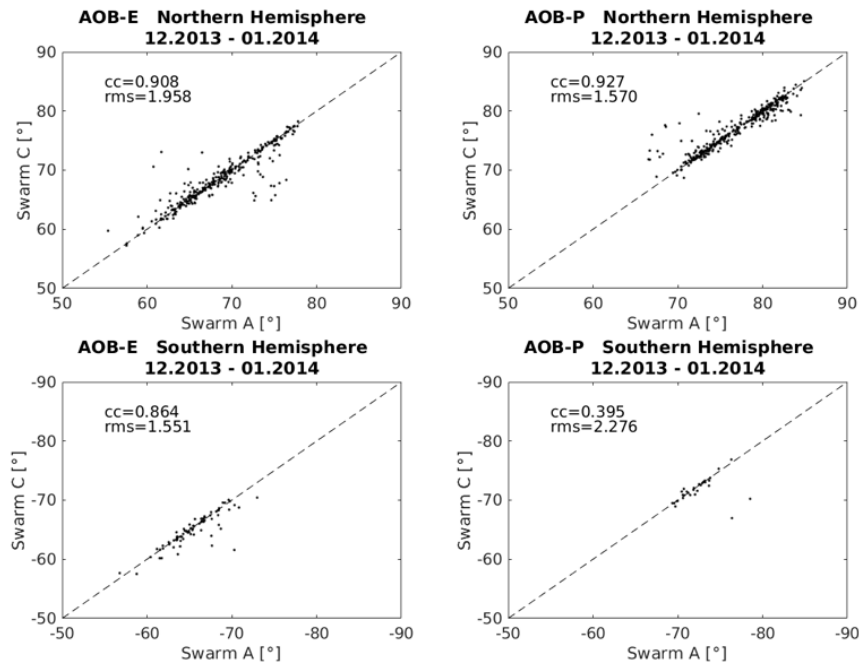


Figure 14: The (left) equatorward and (right) poleward auroral boundaries derived from Swarm-A and Swarm-C in the (top) northern and (bottom) southern hemispheres, respectively. The correlation coefficient (cc) and the root-mean-square difference (rms) are shown in each panel.

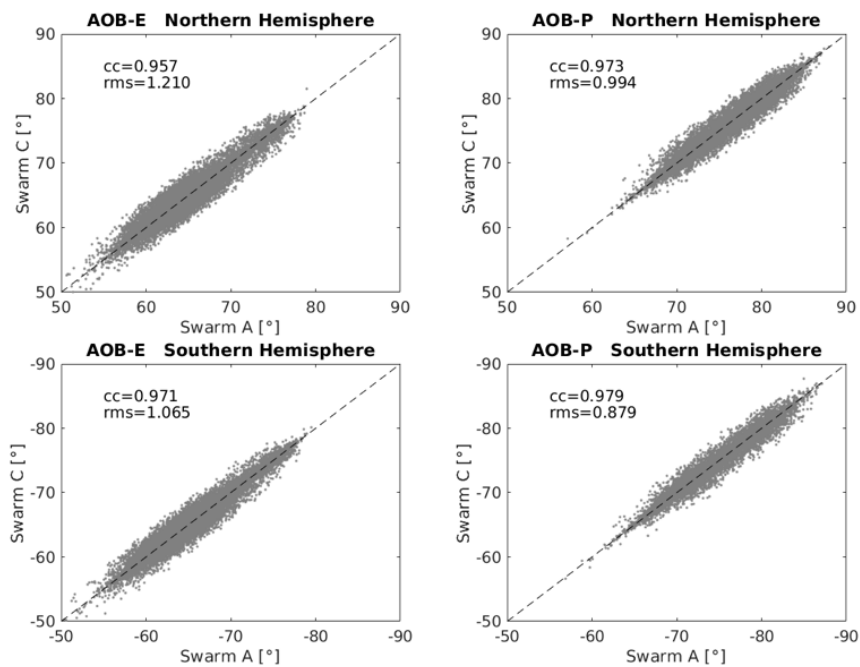


Figure 15: As Fig. 14, but for the results between Swarm-A and Swarm-C during the final constellation period in 17 Apr 2014 to 31 Dec 2018, when the two satellites are flying side-by-side.

4.2 Validation with independent reference material

4.2.1 Validation of LC estimates with AMPS model values

The AMPS (Average Magnetic Field and Polar Current System) model [RD 6] is a climatological model of polar ionospheric current systems determined from CHAMP and Swarm satellite magnetic observations. It provides ionospheric currents at a given position as continuous functions of solar wind speed, interplanetary magnetic field, F10.7 solar flux index, and dipole tilt angle.

We used AMPS to calculate synthetic values $\Delta\mathbf{B}(t)$ of magnetic field disturbances along the orbits of the Swarm-A satellite for June 2015, using driving parameters (solar wind, IMF and F10.7) from the OMNI data base for the time instants t in consideration.

The scalar field signature $\Delta F(t) = \Delta\mathbf{B}(t) \cdot \mathbf{B}_{MF}/|\mathbf{B}_{MF}|$ of the ionospheric currents were calculated by projecting the AMPS magnetic field vector disturbance $\Delta\mathbf{B}(t)$ on the direction of the ambient magnetic field \mathbf{B}_{MF} as given by the CHAOS-6 [RD 3] core field model. We then applied the line-current method to ΔF and estimated the ionospheric sheet current density on an orbit-by-orbit basis.

The top panel of Figure 16 shows, for the Northern hemisphere, the East-West (in the QD frame) component of the ionospheric sheet current density as given by the AMPS model, while the bottom panel shows the sheet current determination as found by applying the Line Current method to the synthetic magnetic data.

The upper part of each panel represent the nightside part of the orbits, whereas the lower part corresponds to the dayside part. Note the slightly positive (i.e. Eastward directed) sheet current density near the equatorward boundary of the nightside oval crossing (which are given in the top part of each panel), in agreement with the results found by analysing actual Swarm magnetic field data (cf. Fig. 35 in Sect. 4.3.2). This is seen in the AMPS currents as well as in the results obtained with the LC method. Figure 17 gives a similar comparison for the Southern hemisphere.

We consider the generally good agreement between the original sheet current density (upper panel) and its estimation using the LC method (bottom panel) as a successful validation of the LC method.

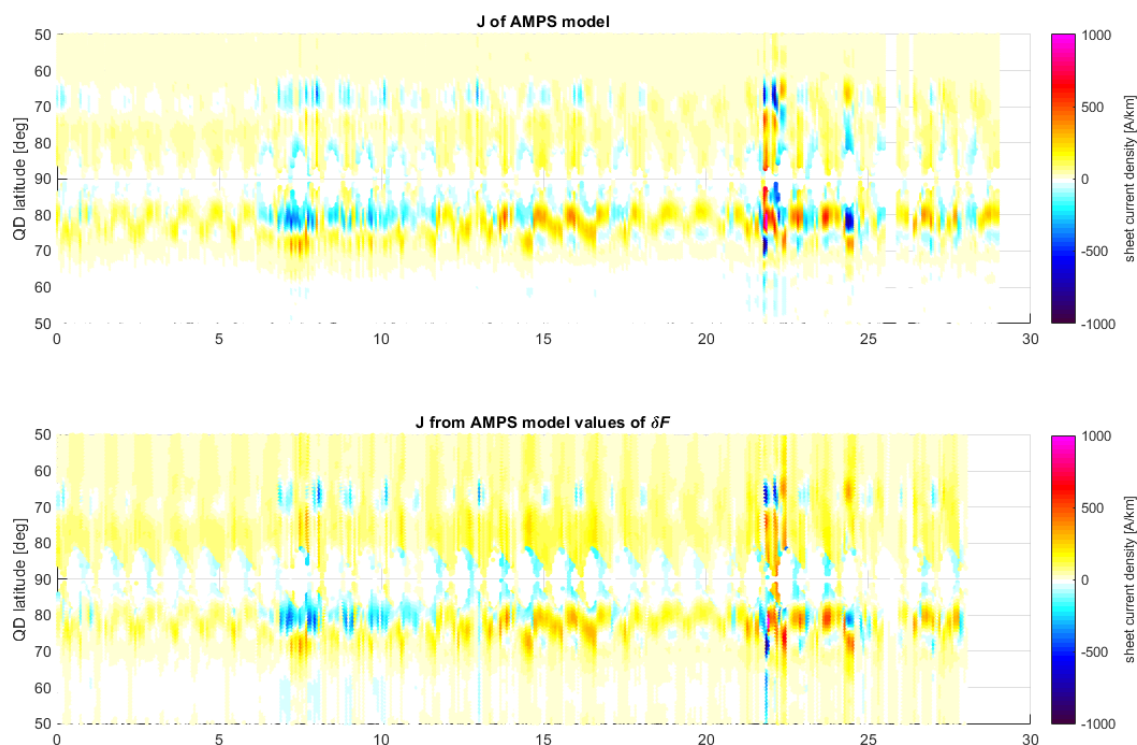


Figure 16: Time-latitude plots of Northern hemisphere sheet current density for June 2015, as given by the AMPS model (top) and estimated from synthetic AMPS magnetic field data using the LC method (bottom)

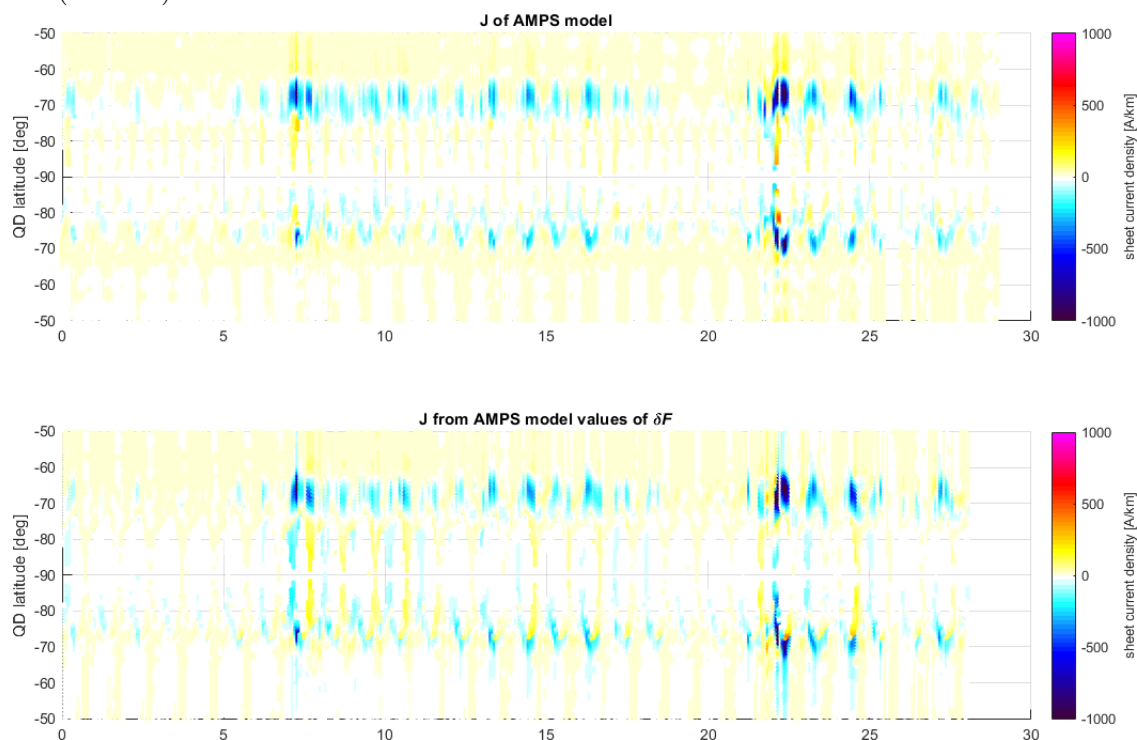


Figure 17: Similar to Fig. 16 but for the Southern hemisphere.

4.2.2 Comparison of SECS estimates with ground-based magnetometer data

Ground magnetometer recordings provide continuous time series that can be compared to Swarm results in two straightforward ways. The first one uses the ground field calculated from the modelled divergence-free ionospheric horizontal sheet current. We remind that the curl-free horizontal current together with the associated radial currents do not produce any magnetic field on the ground.

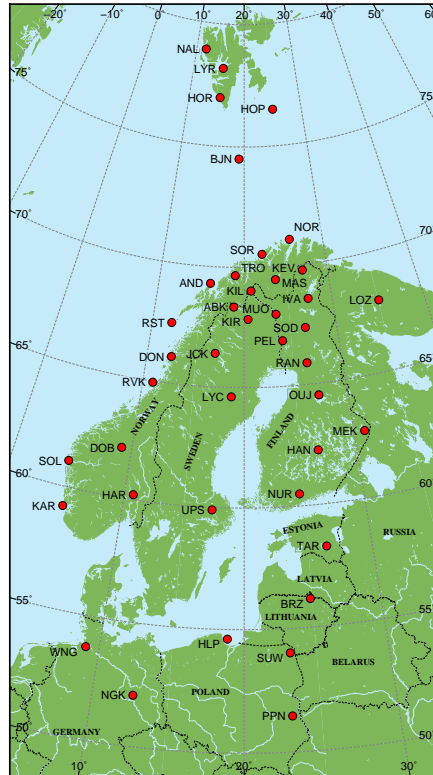


Figure 18: IMAGE magnetometer network (<https://space.fmi.fi/image/>).

We use IMAGE magnetometer recordings from North Europe covering an extensive range of latitudes (Fig. 18) from 51.5 deg to 79 deg. Since the magnetic field calculated from Swarm represents fast variations, the quiet time baseline must be subtracted from the IMAGE data. This has been made simply by selecting visually a quiet period for each day, which is accurate enough for initial comparisons. We have used the geodetic north component (X) of the magnetic field. In the IMAGE region, it is close to the magnetic north component.

Contrary to other parts of this report, we have used the POMME-9 baseline field for Swarm, which means that the magnetospheric contributions are not subtracted from the magnetic field recorded by Swarm. This is consistent to using ground magnetometer data from which only a quiet time baseline has been subtracted without trying to eliminate the magnetospheric part.

Five examples of the magnetic field profiles are shown in Fig. 19. Both Swarm-A ja Swarm-C are used. Since the spacecraft flow very close to each other, differences in the current densities and magnetic fields are nearly insignificant. The first two cases in Fig. 19 demonstrate an overflight under quite stable ionospheric conditions. The largest contribution to the ground magnetic field comes from a westward electrojet close to which the horizontal ground field points about to the south. Despite a small change in the amplitude of the field during the overflight, as indicated by the black and red arrows, its direction has been nearly constant. The most stable example is the overflight on 8 June 2015 at 23:19 UT. Variations in the ground field during the overflight are very

small especially in the region with the largest field values. Swarm has crossed IMAGE in the west where the ground variations are smaller than in the central area of the magnetometer network. Consequently, this leads to slightly underestimated ground field values when determined from the ionospheric current based on Swarm recordings.

In the third event, the ground field experiences quite large changes in its magnitude and some turning in its direction at the northernmost stations. However, Swarm can still detect two clear electrojets, although there is a clear underestimation of the ground field below the westward current.

The fourth example is more complex with an eastward current derived from Swarm at high latitudes, and nearly zero currents elsewhere. However, the ground magnetic field suggests a clear westward current peaked at about 75 deg N and an eastward current only above the northernmost part of IMAGE. As the left-hand-side plot shows, there were notable variations in the ground field at some northern stations with about 90 degrees turning of the horizontal field vector at two sites. So the 1D assumption is obviously not well satisfied in this case.

An especially problematic event is illustrated in the fifth example. Majority of IMAGE horizontal field vectors are nearly transverse to the Swarm orbit indicating that ionospheric currents have been parallel to the orbit. Additionally, the orbit is quite parallel to the magnetic meridian. In the south, there are a few magnetometer stations with the horizontal field having a large component nearly to the south. They can be explained by a westward ionospheric current, but then the ground field at more northern sites remains poorly reproduced. In this case, the relative difference of the maximum current density between A and C satellites is the largest of the five examples, but still quite small (C gives a smaller value of about 5%).

We note that the quality flag of the fifth example has its best value (all zeros). This means that both the eastward and westward electrojet are formally properly identified. Only the direct comparison to ground-based data reveals that this is not the case. Consequently, the quality flag does not provide a sufficient condition for a good determination of ionospheric currents.

For the fifth example, the rms error of the fitted parallel magnetic field at Swarm's altitude is 30.2 nT and the corresponding confidence value is 0.79. As discussed in Sect. 4.1.2, the confidence value equal to or larger than 0.90 evidently indicates an optimal case of the SECS method. So the value of 0.79 implicates that caution is needed, and as the independent ground magnetometer data show, this is not a 1D case.

To reduce possible inaccuracies in the determination of the quiet time baseline, we consider the range of the field: $R_X = \max(X) - \min(X)$. For IMAGE, the value is taken at the closest time step to the median time of the Swarm oval crossing. The median longitude of the Swarm ionospheric footprint must also be close enough to the median longitude of the available IMAGE stations (± 20 deg). Results for Swarm-A are shown in Figs. 20-21. If data from the IMAGE stations are taken at the time step when Swarm is closest to a specific station then the result is practically the same. Figure 22 shows the distribution of R_X differences during magnetically disturbed periods, when the mean time R_X has been larger than 100 nT. The average relative difference is 0.94% and the standard deviation is 19.7%.

For comparison, we also derived the same statistical results with Swarm data of which the magnetospheric contribution was subtracted (plots not shown here). Compared to Fig. 20, the slope decreased a little to the value of 0.676. Compared to Fig. 21, the ratio of R_X of Swarm to IMAGE decreased to 0.91 for the mean value and to 0.78 for the median value. Since these changes are rather small, the precise selection of the baseline field model for Swarm is not critical.

We note that the ground magnetic variation field is a sum of two parts. The external (or primary) field is produced by currents in space, and the internal (or secondary) field is due to currents induced in the conducting ground. As a rule of thumb, the internal field tends to increase the horizontal field and decrease the vertical component. The internal contribution can sometimes

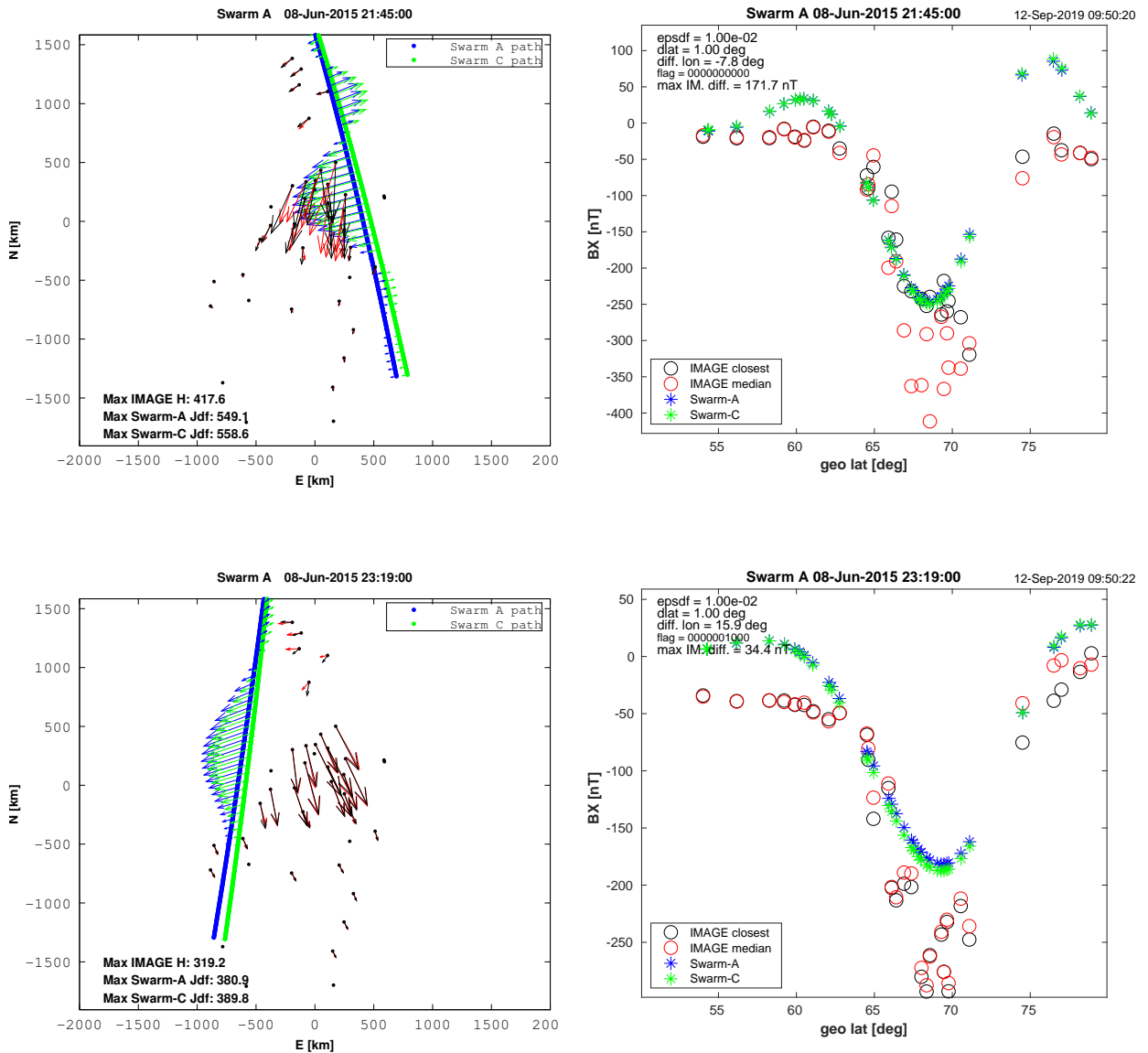


Figure 19: Left-hand-side plots. Blue and green arrows: divergence-free current density J_{df} by Swarm-A and Swarm-C. For clarity, arrows start from the path of Swarm-A. Black arrows: horizontal ground magnetic field at the time when Swarm has been closest to the corresponding IMAGE magnetometer station. Red arrows: horizontal ground magnetic field at the median time of the Swarm overflight. Right-hand-side plots. Blue asterisks: modelled northward ground magnetic field B_x based on J_{df} by Swarm. Black circles: IMAGE B_x at the time when Swarm has been closest to the corresponding magnetometer station. Red circles: IMAGE B_x at the median time of the Swarm overflight.

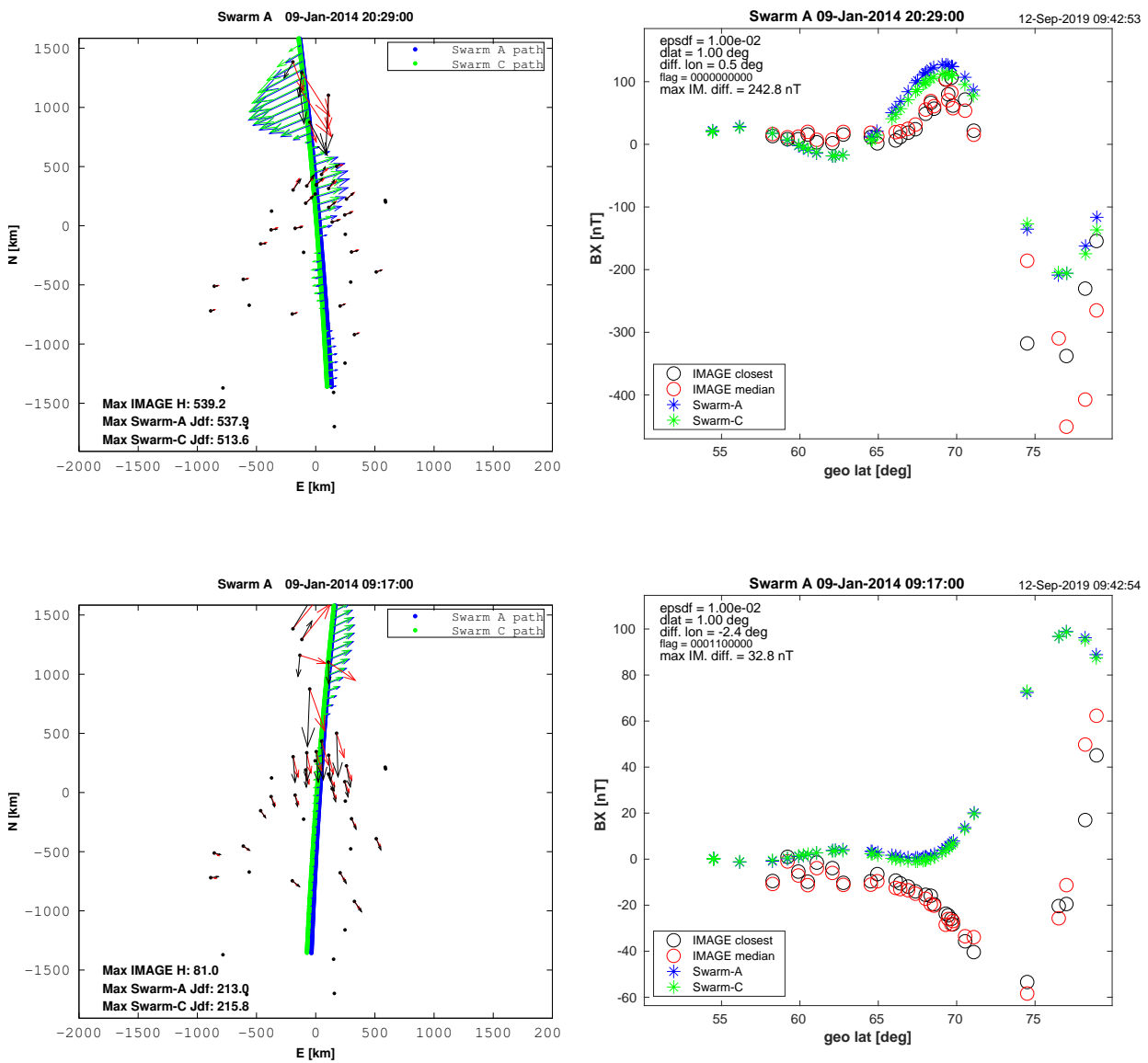


Figure 19a: Fig. 19 continued.

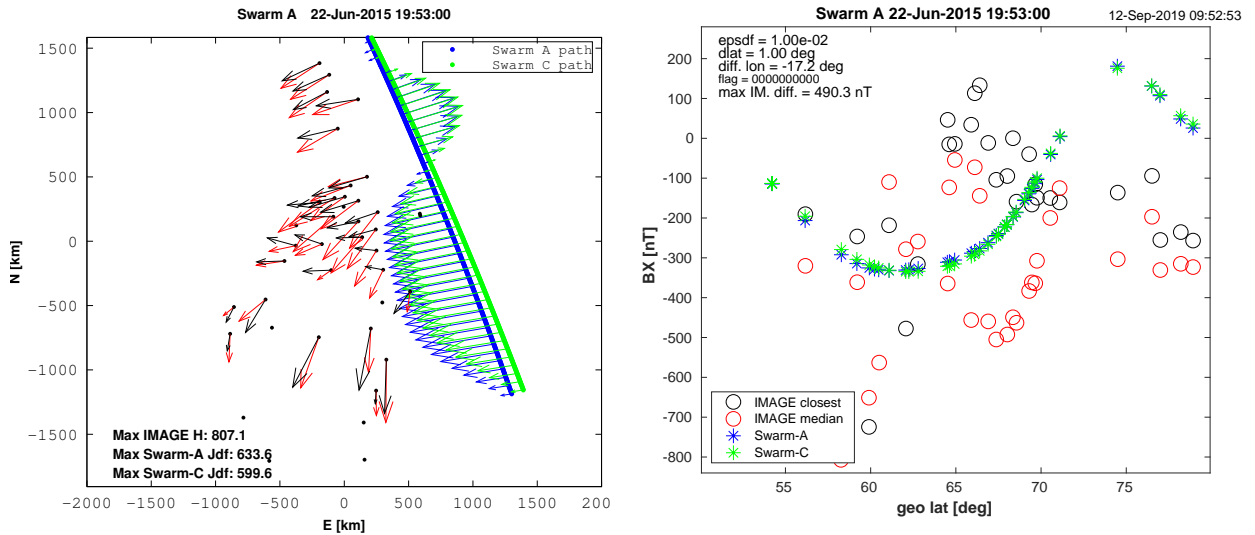


Figure 19b: Fig. 19 continued.

be notable [RD 9]. In principle, it is mathematically possible to separate these contributions. For the magnetic field comparison, we have not done this. However, the following subsection for another type of comparison applies the separation.

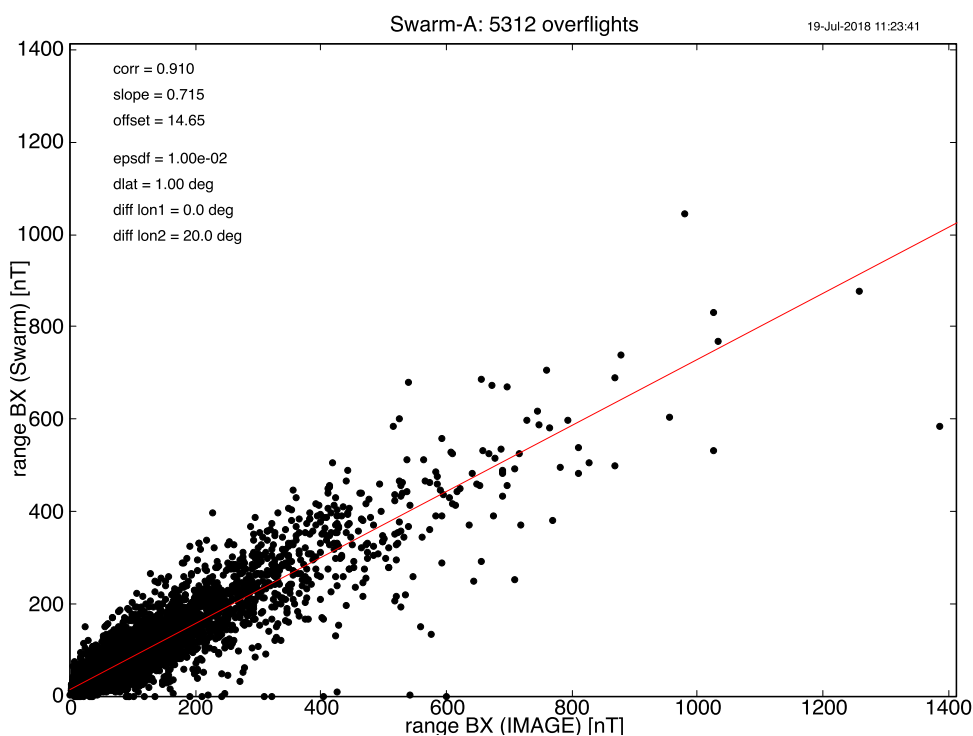


Figure 20: Range R_X of the north component of the ground magnetic field as observed by IMAGE and modelled from Swarm in Dec 2013 to Apr 2018 for oval crossings that occurred within ± 20 deg from the median IMAGE longitude.

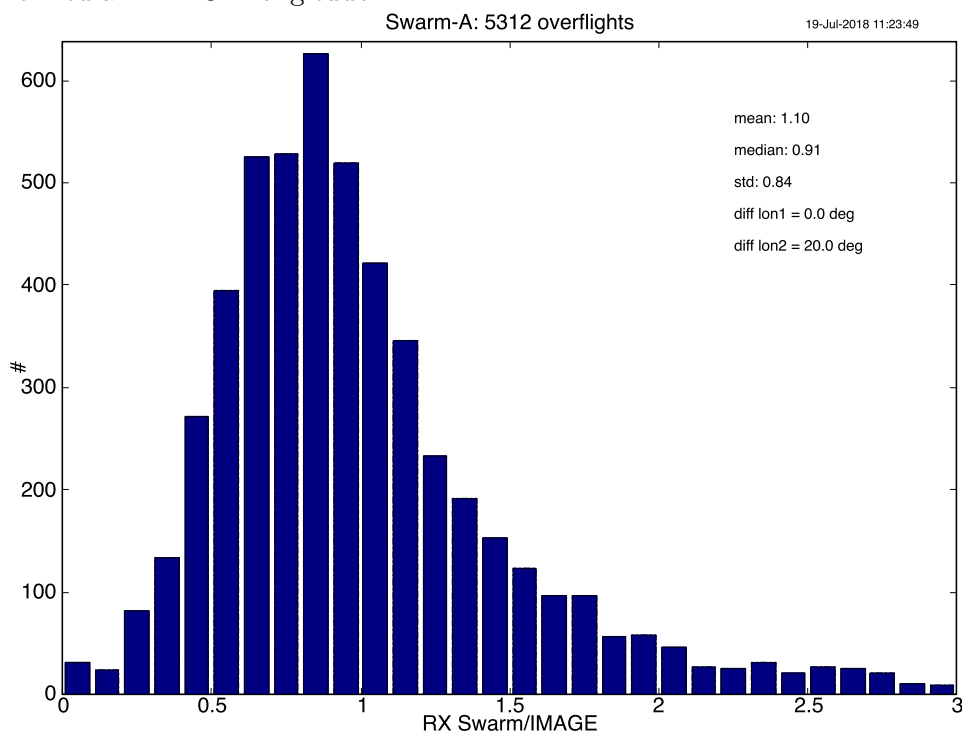


Figure 21: Ratio of R_X of Swarm to IMAGE. The same data are used as in Fig. 20.

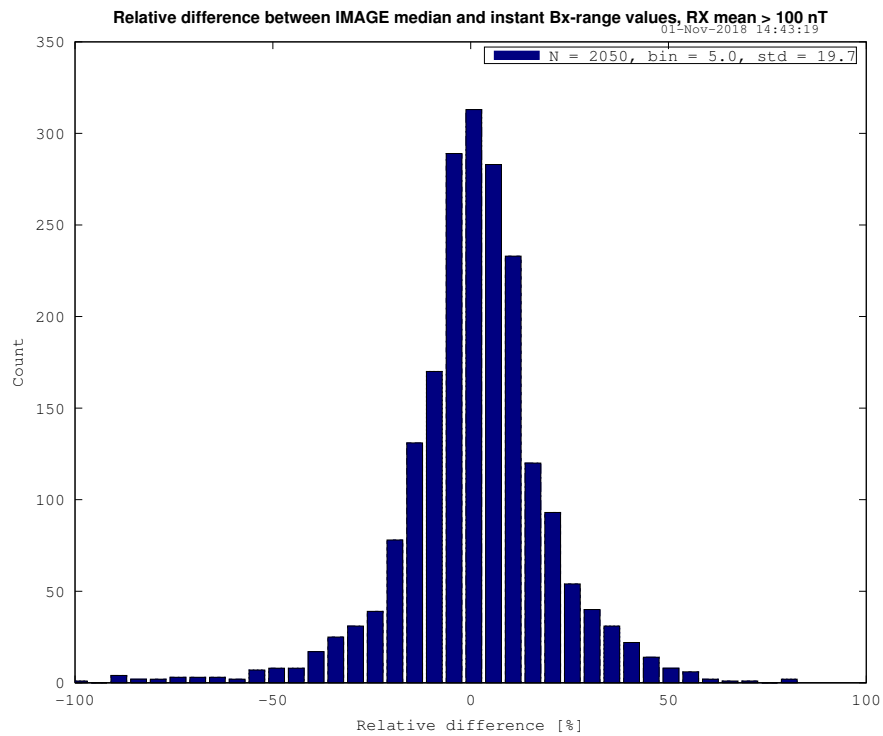


Figure 22: Relative difference between instant and mean IMAGE R_X values during Swarm-A overflights in 2013-2018 when the mean time R_X was larger than 100 nT. The average difference is 29.8 nT.

4.2.3 SECS estimates and equivalent currents derived from the ground magnetic field

Additionally to the comparison of the measured ground magnetic field with the modelled field by Swarm, as presented above, it is also possible to consider ionospheric currents. Ground magnetometer recordings can be converted to ionospheric equivalent currents (J_{eq}) as described by [RD 2]. This is a divergence-free horizontal sheet current and thus comparable to J_{df} obtained from Swarm recordings.

As discussed above, the measured ground magnetic field is the sum of the external and internal fields. [RD 4] showed that the best results for satellite comparisons are obtained when the internal field is removed. This is feasible when a two-dimensional magnetometer is available as is the case for IMAGE at least when its continental part is considered.

The main difference between the two comparisons is that the first one uses ground magnetic field recordings as such, whereas the second one converts them to equivalent ionospheric currents. The latter involves more assumptions due to the need to select parameters for the SECS method when applied to the ground data. Additionally, the IMAGE network is only a chain in its northernmost part, which reduces the resolution of 2-D features there. We note that all three components of the ground magnetic field are used if the external part is separated before calculating the equivalent currents. Without the separation, only the horizontal components can be used. Following [RD 4], the ionospheric current sheet is set at the altitude of 110 km equivalently to Swarm. Theoretically, 100 km would be better for ground magnetometer data, since there are currents below 110 km. The sheet current representing induced currents in the ground is set just below the surface (0.01 km). This is an optimal choice, since especially high-frequency induced currents concentrate close to the surface. All available magnetometer stations are used for deriving the equivalent currents.

Two examples of the modelled current densities are presented in Fig. 23. The case in the left plot shows very good similarity between Swarm and IMAGE especially in the dense continental part of the magnetometer network south of the DIP latitude 68. The example in the right plot demonstrates how IMAGE estimates incorrectly the precise location and magnitude of the minimum of the westward current occurring above the Arctic Ocean, where there are only five magnetometer stations. Both examples illustrate that the current estimate based on the external part of geomagnetic variations is generally smaller than the current obtained from the total variation.

It is also possible to calculate the equivalent currents exactly at the ionospheric footprints as shown in Fig. 24. For the Swarm overflight at 21:45:00 UT, there is only a small difference to Fig. 23, whereas the difference is clearly larger at 23:19:00 UT. This can be due to the failure of the 1D assumption and/or the larger distance of the orbit from IMAGE than at 21:45:00 UT.

Statistics using the minimum and maximum current densities shows a high linear correlation between IMAGE and Swarm (Figs. 25-26). When the equivalent currents from IMAGE are estimated from the external part of the ground magnetic field, the slope of the straight line fitted to the data points is very close to unity. When the total horizontal variation field is used, the slope is smaller, or in other words, IMAGE tends to yield larger currents densities than Swarm. This is evidently due to the effect of induced currents in the ground that increase the horizontal field as discussed previously and thus IMAGE overestimates the equivalent currents.

When the slopes of the straight lines are compared between Figs. 25 and 26, they are larger in the latter case, in which equivalent currents from IMAGE are calculated at the footprints of Swarm. It is an intrinsic feature of the SECS method that equivalent currents decrease smoothly towards zero outside of the analysis area. Since the SECS grid only covers the region of the magnetometer network with a small spatial extension, equivalent currents far from IMAGE can be underestimated.

Another comparison uses the total amplitudes of eastward and westward currents across IMAGE latitudes determined from IMAGE and Swarm (Figs. 27-28). In this case, the amplitudes are

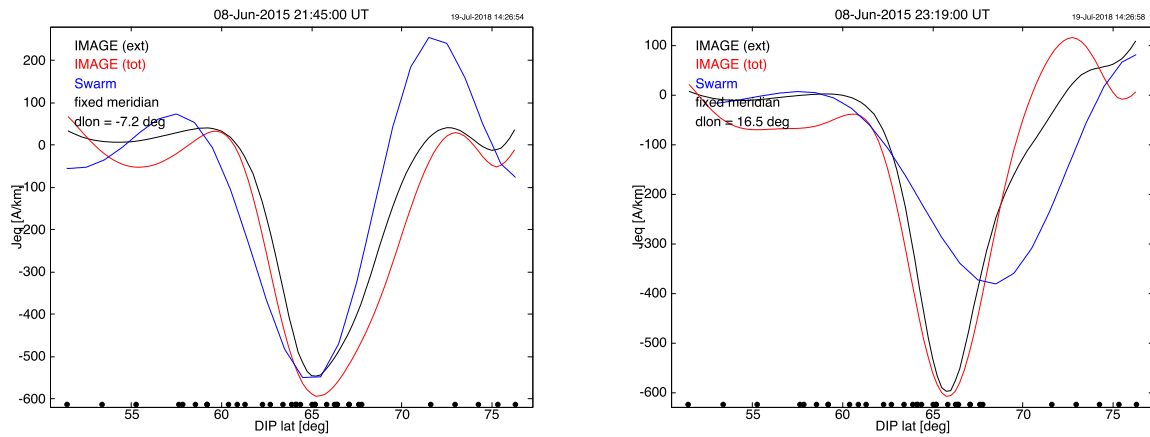


Figure 23: Modelled divergence-free horizontal ionospheric current density for two Swarm-A crossings over the IMAGE magnetometer network (the same as in Fig. 19). The current derived from Swarm is plotted in blue. The equivalent current derived from IMAGE with the external field separation in black, and without the field separation in red. The small black dots on the horizontal axis show the locations of the available IMAGE stations. The DIP latitude is given with respect to the QD north pole and the current flows transverse to the DIP meridians. The current density derived from IMAGE is calculated along a DIP meridian from South Finland to Svalbard. The difference between the median longitude of the magnetometer stations and the median longitude of the ionospheric footprints is d_{lon} .

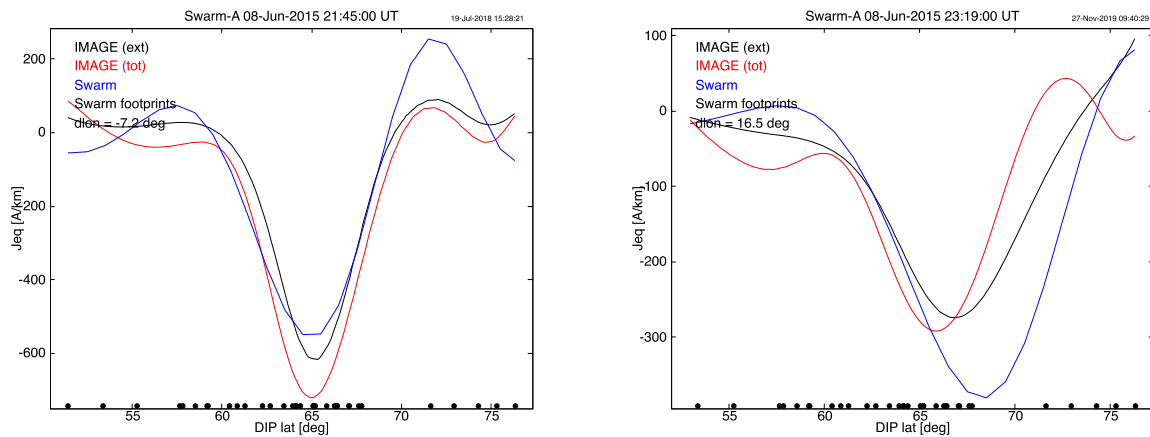


Figure 24: As Fig. 23, but the current densities derived from IMAGE are calculated at the ionospheric footprints of Swarm.

calculated taking into account the full latitude range of IMAGE instead of the sequences that define the main electrojets as in Fig. 3. Since the analysis area for Swarm covers a large region (50 to 85 deg in QD latitudes), it is reduced to the same range as IMAGE provides.

There are several crossings during which Swarm indicates a very small electrojet (close to zero) whereas IMAGE shows a large amplitude (larger than 100 kA), or vice versa. Figure 29 illustrates events with large differences. We note that in these cases Swarm has flown close to the central meridian of IMAGE, so the distance between observations should not cause deviations. Sometimes the reason for them is clearly a bad selection of the quiet time baseline, but this does not concern all cases. An obvious explanation in many cases is a failure of the 1D assumption.

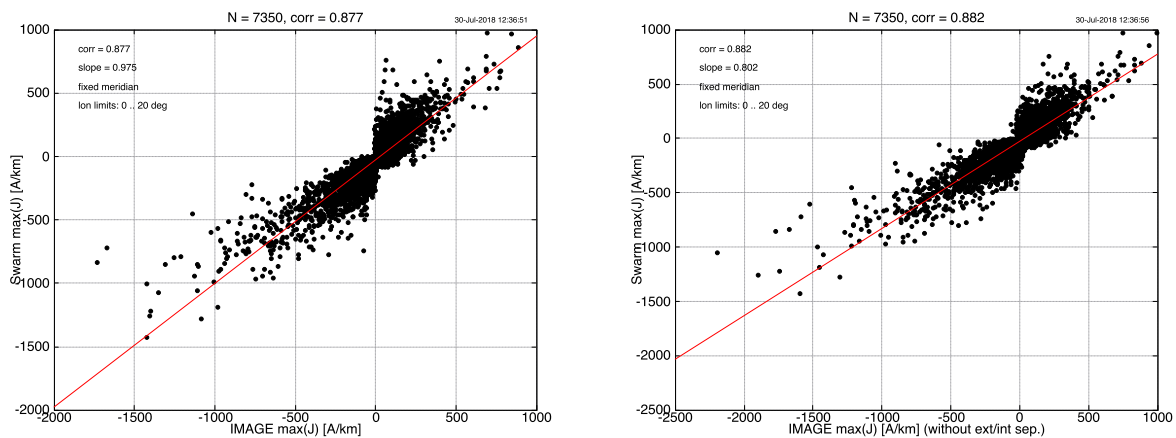


Figure 25: Modelled divergence-free horizontal ionospheric current density during Swarm crossings over the IMAGE magnetometer network in Dec 2013 to Apr 2018. The current density derived from IMAGE is calculated along a DIP meridian from South Finland to Svalbard. From each crossing, the minimum and maximum current density is considered (i.e. two values for each crossing). Left: the external magnetic variation field of IMAGE is used. Right: the total magnetic variation field of IMAGE is used. All oval crossings that occurred within ± 20 deg from the median IMAGE longitude have been included. The red line shows the linear fit.

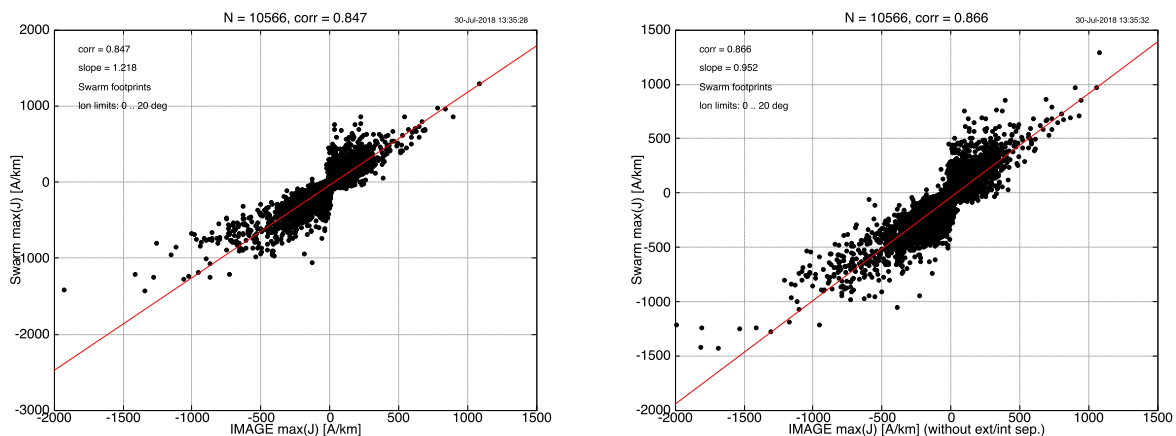


Figure 26: As Fig. 25, but the current density derived from IMAGE is calculated at the ionospheric footprints of Swarm.

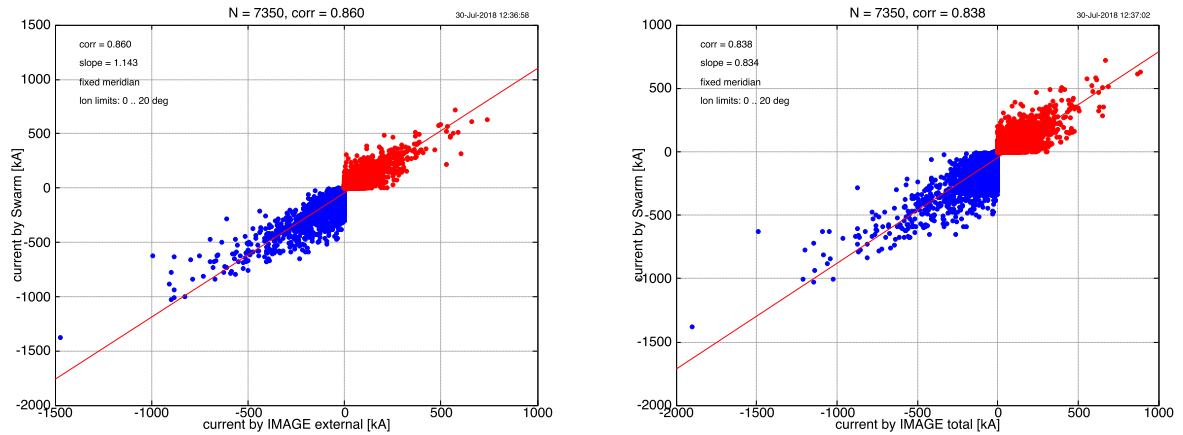


Figure 27: Modelled divergence-free horizontal ionospheric eastward (red) and westward (blue) currents during Swarm crossings over the IMAGE magnetometer network in Dec 2013 to Apr 2018. The current density derived from IMAGE is calculated along a DIP meridian from South Finland to Svalbard. Left: the external magnetic variation field of IMAGE is used. Right: the total magnetic variation field of IMAGE is used. All oval crossings that occurred within ± 20 deg from the median IMAGE longitude have been included. The red line shows the linear fit.

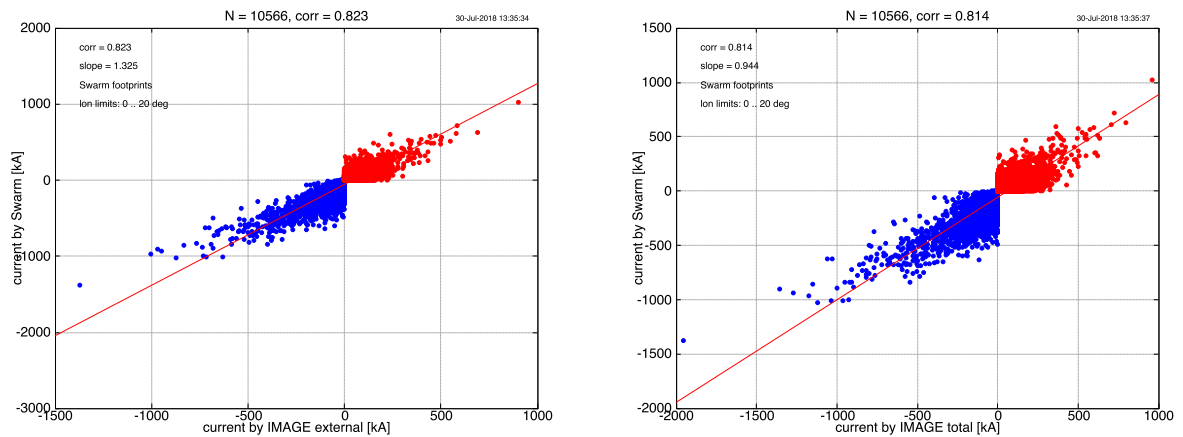


Figure 28: As Fig. 27, but the current density derived from IMAGE is calculated at the ionospheric footprints of Swarm.

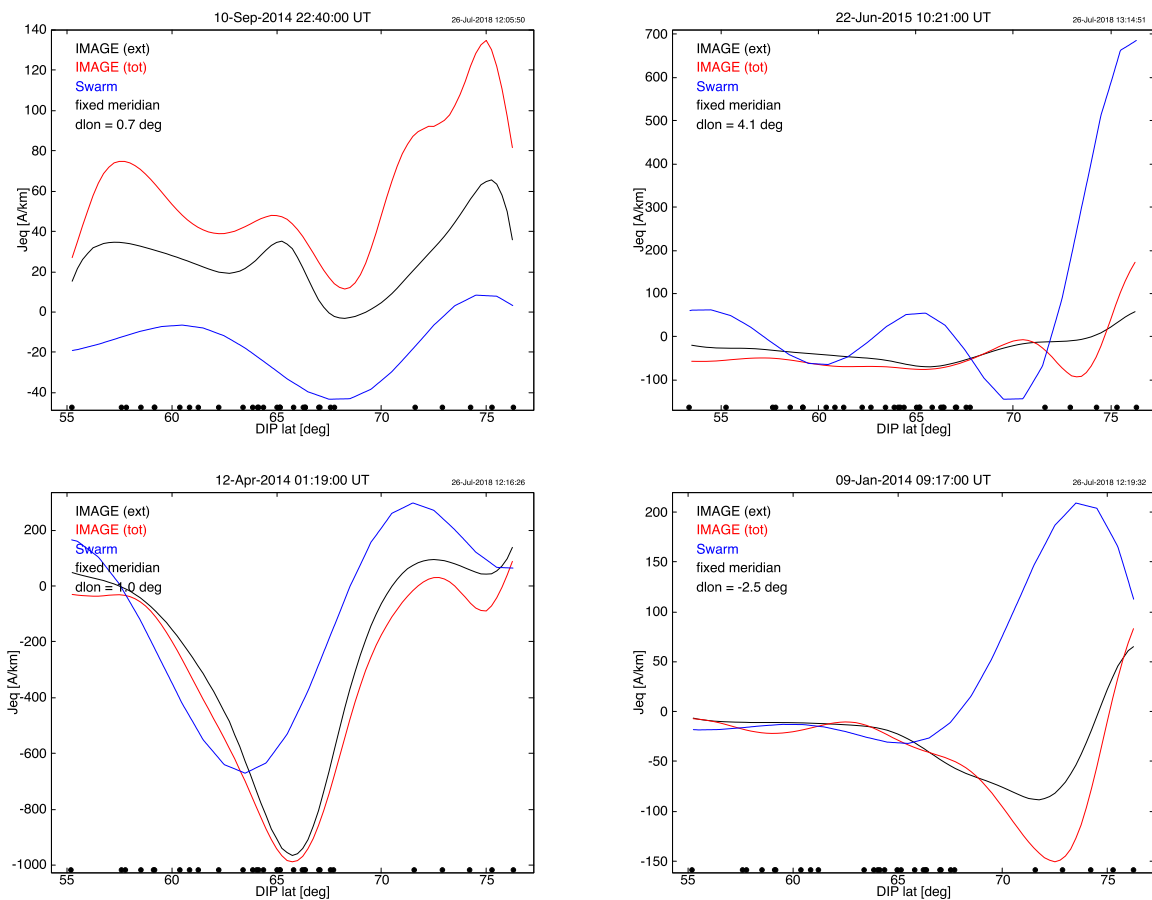


Figure 29: Examples of Swarm crossings over IMAGE with large differences in the modelled divergence-free current density. The small black dots on the horizontal axis show the locations of the available IMAGE stations.

4.2.4 AOB vs DMSP

Auroral oval boundaries have also been derived by using the precipitating electron and ion measurements of the Defense Meteorological Satellite Program (DMSP) satellites [RD 5]. The dataset includes the results for three DMSP satellites, F16-18, during the five year period in 2010 to 2014. As there is a 1-year overlap in 2014 between the Swarm and DMSP satellites, it is worth comparing the derived AOB products between the satellites when they were flying close together. Using Swarm-A and DMSP F18 satellites as an example, the derived AOB products are quite consistent between the two satellites (Fig. 30). Only events with the UT difference less than 6 min and MLT difference less than 15 min have been taken into account.

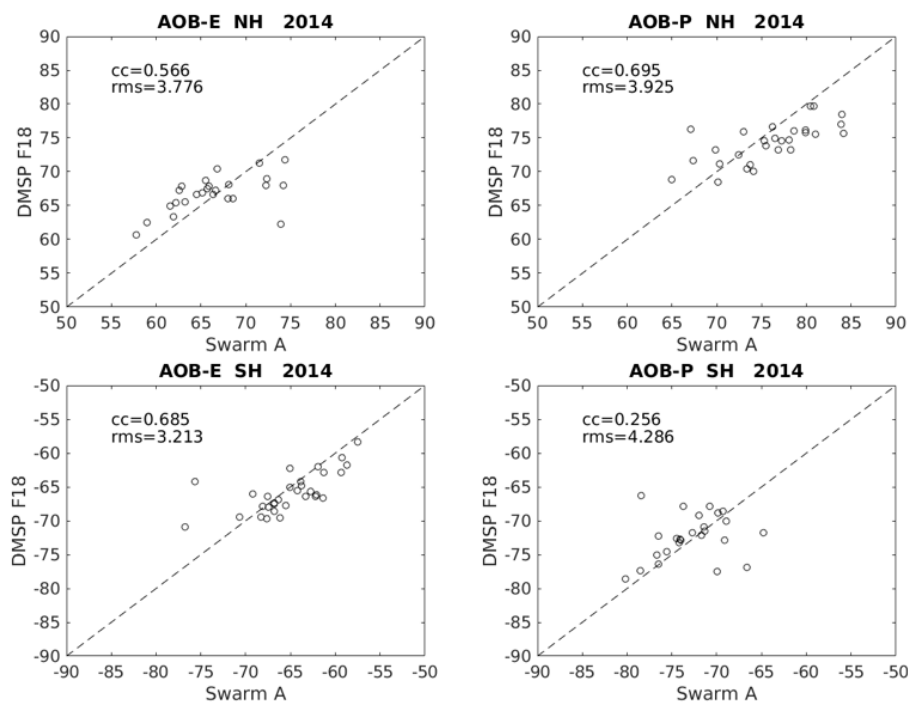


Figure 30: The (left) equatorward and (right) poleward auroral boundaries derived from Swarm-A and DMSP F-18 satellites in the (top) northern and (bottom) southern hemispheres, respectively. The correlation coefficient (cc) and the root-mean-square difference (rms) are shown in each panel.

In the following, we have compared the peak locations between large-scale (>150 km) FACs and precipitating electron/ion energy flux measured by the DMSP satellites. FACs and precipitation data used are from DMSP F16, F17 and F18, during a five-year period in 2010 to 2014 [RD 13].

Figure 31 shows latitudinal profiles of DMSP FACs (black), energy flux of electrons (blue) and ions (red) along the dusk-dawn meridian and averaged within ± 1.5 h MLT. The solid and dashed lines represent the values in the northern and southern hemispheres, respectively. The left and right columns show results for intense northward ($5\sim 10$ nT) and southward ($-10\sim -5$ nT) IMF B_z , respectively, and with varying B_y condition for each subpanel. For visualization purposes, the values of electron and ion precipitations have been divided by factors of 1×10^{12} and 1×10^{11} eV/cm²/ster/s, respectively. The intensity of all three quantities increase and they cover a more equatorward latitudinal range for southward B_z than for northward B_z . For northward $B_z > 5$ nT, however, it is not straightforward to reliably separate the R1/R2 current along the dusk-dawn meridian, though the peaks of precipitating electrons and ions are well discernible. Therefore, the following comparison between FACs and precipitation will be conducted for $B_z < 5$ nT. The

intensity of the ion flux is in average stronger on the dusk side, while the intensity of the electron energy flux is stronger in the dawn side. The peaks of the electron energy flux at the dusk and dawn sides are located around 70° MLAT and 64° MLAT, while the peaks of the ion energy flux are located around 65° and 68° MLAT, respectively. In the following, peaks of all three quantities are identified, as is demonstrated in Fig. 32 for the lower right panel of Fig. 31. As expected, the locations of the peaks of the upward FACs correspond well to the peaks of the electron energy flux, and the location of the peaks of the downward currents correspond well to the peaks of the ion energy flux.

Table 2 shows the MLT locations of the peaks of upward/downward FACs and electron/ion energy flux for all subpanels with $B_z < 5$ nT, separately for the dusk and dawn sides as well as the two hemispheres. Table 3 shows the mean difference of all entries in Table 2, separately for the dusk and dawn sides and the two hemispheres. Positive values reflect that the electron/ion energy flux peak is located poleward of the upward/downward FACs peak, and negative values reflect its equatorward location. On average, larger differences occur between the locations of R1 currents and ion/electron flux peaks (especially at the dawn side), than for R2 currents. At R1 the particle flux peaks are poleward of the FAC peaks, while at R2 the particle flux peaks are equatorward of the FAC peaks.

Figure 33 visualizes the mean locations of these peaks. The red/blue thick lines represent the upward/downward FACs, and the dot/cross within black circles represent the precipitation electron/ions, respectively. Interestingly, the FAC peaks enclose the particle energy flux peaks at both dusk and dawn side and in both hemispheres.

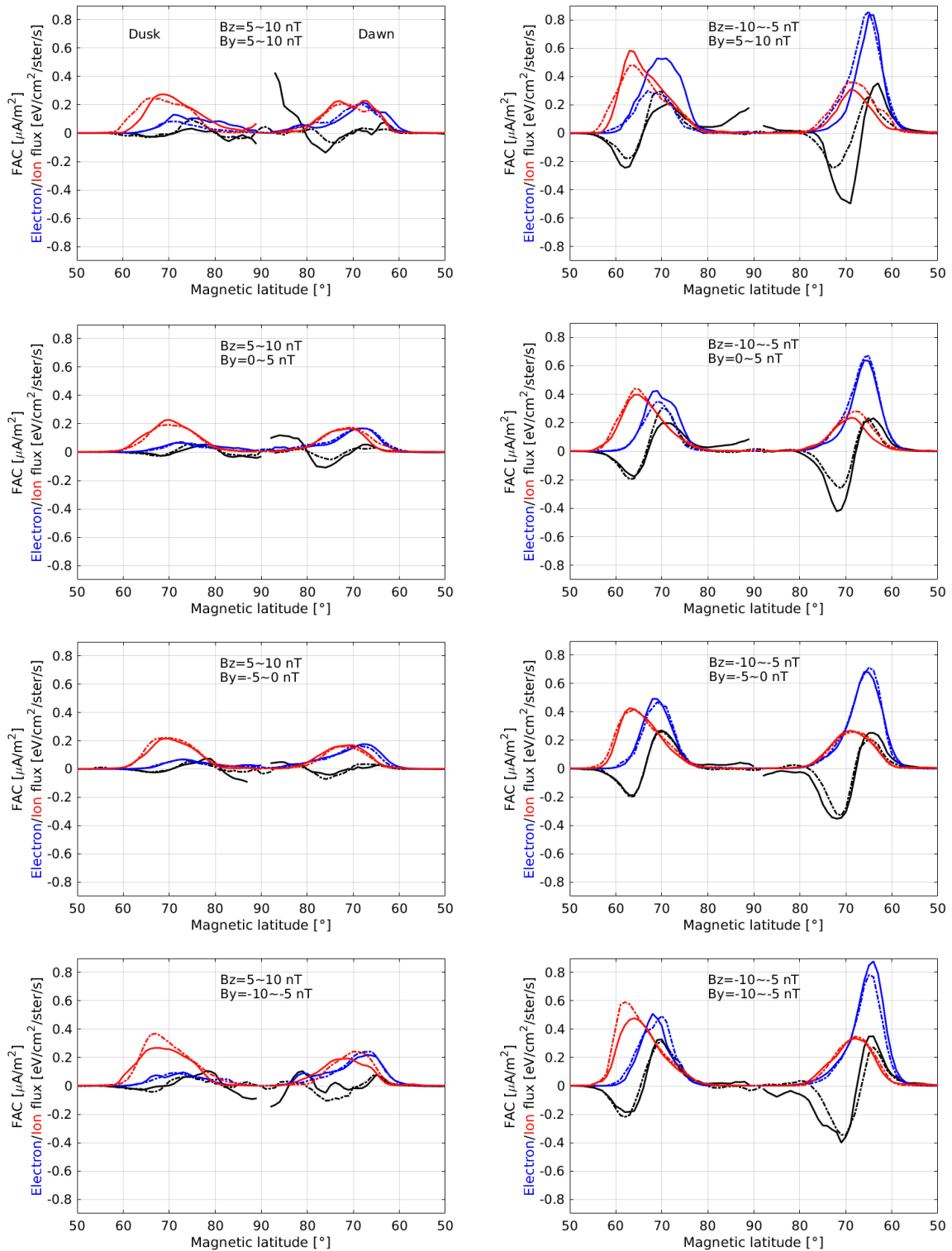


Figure 31: The latitudinal profiles of FACs (black) and electron (blue) and ion (red) energy fluxes. The quantities are averaged within ± 1.5 h MLT centered on the dusk-dawn meridian. The solid and dashed lines represent the values in the northern and southern hemispheres, respectively. Here we show only the results for the more northward (left, $B_z = 5 \sim 10$ nT) and more southward (right, $B_z = -10 \sim -5$ nT) IMF B_z conditions [RD 13].

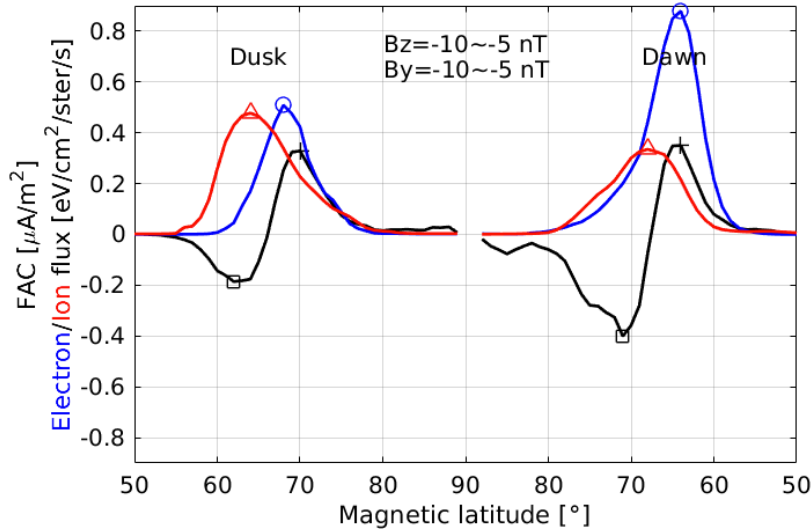


Figure 32: The latitudinal profiles of FACs (black), electron (blue) and ion (red) energy fluxes in the northern hemisphere with IMF B_z and B_y both within $-10\sim-5$ nT. For both dusk and dawn sides, the upward and downward peaks of FACs are marked with black cross and rectangle, while the peaks of electron and ions energy fluxes are marked with blue circle and red triangle, respectively [RD 13].

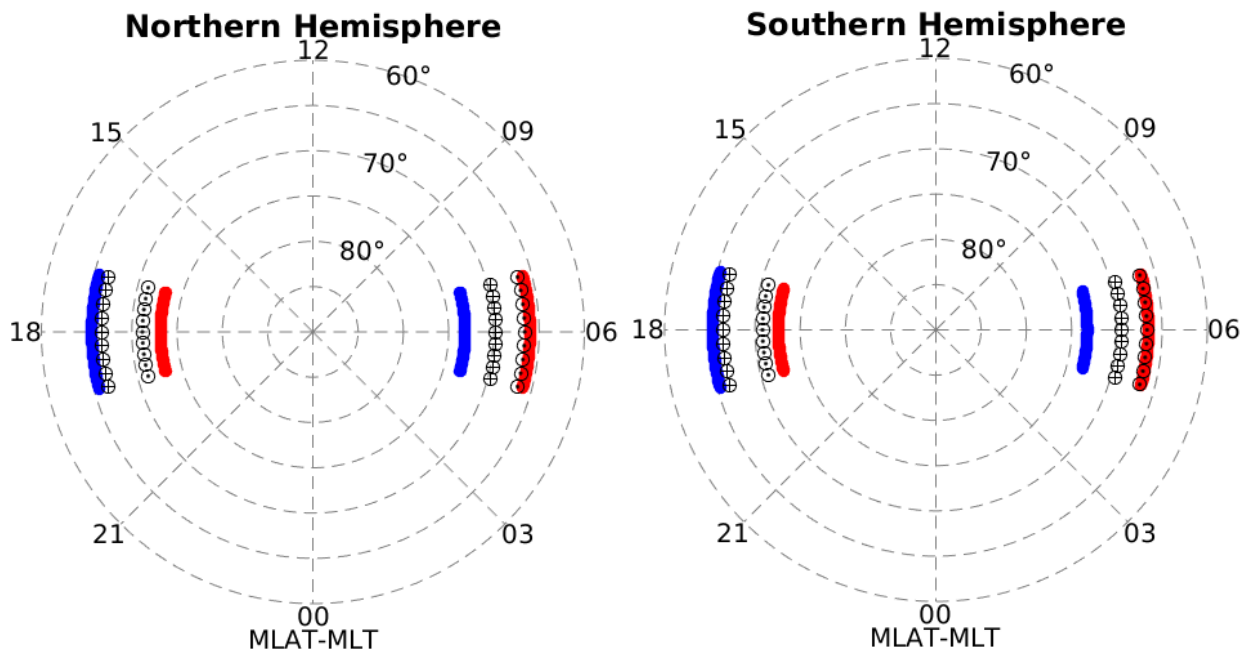


Figure 33: The locations of the peaks of upward (red) and downward (blue) FACs, as well as the precipitation electrons (dot within black circle) and ions (cross within black circle) at dawn and dusk sides, and also in the two hemispheres [RD 13].

Table 2: The MLAT of peaks for upward/downward FAC, electron energy flux, and ion energy flux, separately for the dusk and dawn sides, as well as for the two hemispheres. Only the conditions with IMF $B_z < 5$ nT have been considered [RD 13].

Northern hemisphere									
IMF		Dusk				Dawn			
B_z (nT)	B_y (nT)	Upward FAC (R1)	Downward FAC (R2)	Electron flux	Ion Flux	Upward FAC (R2)	Downward FAC (R1)	Electron flux	Ion Flux
0~5	5~10	74	67	74	68	66	75	67	70
	0~5	76	69	74	69	68	76	68	71
	-5~0	78	68	73	70	68	76	68	71
	-10~-5	74	67	72	68	68	73	68	69
-5~0	5~10	73	66	71	67	66	73	66	70
	0~5	74	67	73	68	67	73	67	70
	-5~0	74	67	72	68	68	74	68	71
	-10~-5	72	65	71	67	66	74	67	70
-10~-5	5~10	72	62	69	63	63	69	64	69
	0~5	71	64	69	65	64	72	66	69
	-5~0	70	63	68	63	64	72	66	69
	-10~-5	70	62	68	64	64	71	64	68
Southern hemisphere									
0~5	5~10	75	67	71	68	68	74	67	70
	0~5	75	68	73	69	68	75	69	72
	-5~0	75	68	73	69	68	76	69	71
	-10~-5	73	66	72	68	67	74	67	70
-5~0	5~10	73	65	71	67	66	74	66	69
	0~5	74	67	72	68	68	74	68	70
	-5~0	74	67	72	68	68	74	68	70
	-10~-5	72	65	71	66	66	73	66	69
-10~-5	5~10	70	63	67	64	65	73	65	69
	0~5	70	63	69	64	65	71	65	68
	-5~0	70	63	69	64	65	71	65	68
	-10~-5	70	62	70	62	64	70	65	68

Table 3: The mean differences between the peaks of electron/ion energy flux and upward/downward FACs separately for dusk and dawn sides and the northern (NH) and southern (SH) hemispheres. Only the conditions with IMF $B_z < 5$ nT have been considered [RD 13].

	Dusk		Dawn	
	Electron flux and upward FAC (R1)	Ion flux and downward FAC (R2)	Electron flux and upward FAC (R2)	Ion flux and downward FAC (R1)
NH	-2.0°	1.1°	0.6°	-3.4°
SH	-1.8°	1.1°	0.2°	-3.8°

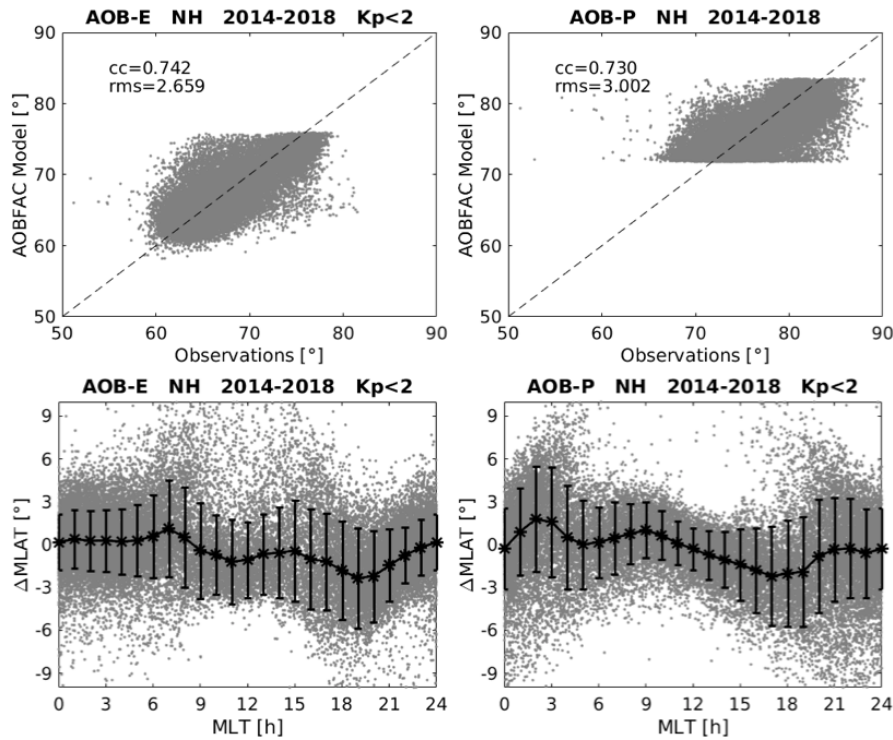


Figure 34: Correlation (top) and difference (bottom) between the empirical model (AOBFAC) predictions and the Swarm AOB product for equatorward (left) and poleward (right) boundaries. Only the results in the northern hemisphere during magnetically quiet periods ($K_p < 2$) are shown.

4.2.5 Swarm AOB product vs empirical AOBFAC model

For validation of GFZ’s empirical model (AOBFAC) [RD 12, 11], we provide the comparison between the model prediction and auroral oval boundary (AOB) product derived from Swarm, as well as the auroral boundary location estimated from DMSP satellites, respectively.

As shown in Fig. 34, we have taken the AOB product derived from the three Swarm satellites during the 5-year period in 2014-2018, to compare with our empirical model predictions. The $\Delta MLAT$ is defined as the model prediction minus the Swarm AOB product, and only the observations during magnetically quiet periods ($K_p < 2$) have been taken into account. Due to the upper limit setting in our empirical model for the solar wind merging electric field value, the auroral oval boundary prediction shows also an upper limit, as seen in Fig. 34.

The model shows generally consistent results with the Swarm AOB product for both the (left) equatorward and (right) poleward boundaries. The median values of $\Delta MLAT$ vary within $\pm 2^\circ$, and the root-mean-square (rms) varies within $\pm 3^\circ$ for all MLT. Relatively large differences are found for the dawn and dusk MLT hours.

As supplementary material, Appendix A.3 compares the AOBFAC model to the DMSP AOB product.

4.3 Cross-comparison between products

4.3.1 LC vs SECS

Figure 35 shows estimated sheet-current densities for June 2015 in dependence on QD-latitude and time as estimated using the SECS method (upper panel, LPS data product), resp. the Line Current (LC) method (bottom panel, LPL data product), for the Northern polar region, estimated from Swarm-A magnetic data. The upper part in each panel represent the nightside part of the orbits, whereas the lower part corresponds to the dayside part. A similar plot for the Southern hemisphere is shown in Figure 36.

The two methods provide consistent estimates of the ionospheric sheet current density, starting from a geomagnetic quiet period during the first days of June 2015 and enhanced geomagnetic activity starting on 7 June. This leads to an equatorial expansion of the ionospheric currents, and the occurrence of negative (i.e. westward) currents in the northern, poleward part. Notable differences appear at the poleward boundary, where the LC methods provides values also above MLAT 85 while SECS does not, and during the storm period of June 22-23. During storm conditions the assumption of 1Dness, which both methods are based on, may fail. Therefore, it is difficult to say which of the methods yields more reliable results during the stormy days.

There seems to be a tendency for slightly positive (eastward) currents near the equatorward boundaries (at around 50° QD latitude) in the Northern hemisphere (Fig. 35). Although this is seen with both methods, it is most prominent in the results of the LC method. Note that these results are derived using magnetic field observations after removal of model values of the core, lithosphere and large-scale magnetosphere, i.e. *assuming* that any remaining magnetic signature is of ionospheric origin. An insufficient removal of e.g. magnetospheric field contributions will necessarily lead to biased estimates of the ionospheric currents.

Ionospheric currents in the Southern hemisphere, shown in Figure 36, are weaker compared to the Northern hemisphere, as it is expected for (southern) winter conditions due to the lower ionospheric conductivity.

Figure 37 shows daily averages of root-mean-squared (rms) data misfit obtained with the two methods, for the Northern (left), resp. Southern (right) hemisphere. The data misfit of the LC method is lower (by about one order of magnitude) compared to the SECS method, probably due to the fact that the latter works with vector data whereas the LC method is based on scalar data. Since vector data is known to be more contaminated e.g. by FACs (in particular the magnetic horizontal components), any such contribution – and in particular FAC contributions at spatial and temporal scales smaller than that captured by the SECS method – will lead to increased rms data misfit. We note that this does not indicate degraded quality of the data product, but it is just a consequence of the methodology and the data that are used.

A statistical comparison between a couple of key output parameters of both methods is shown in Figs. 38-39 using Swarm-A of the year 2015. We note first that the LC method tends to produce a slightly smaller number of oval crossings due to differences in the modelling methods. For example, in the case shown here, the total number of crossings is 22441 for the SECS method and 22385 for the LC method. In the following, we have included only such crossings that have the best quality flag (all zeros) for the SECS method. (As practical guidance, simultaneous crossings by the LC and SECS methods are identified by looking for time stamps with some tolerance.)

Figure 38 shows the peak QD latitude of the electrojets determined by the SECS and LC methods separately for both hemispheres. An excellent correspondence is seen. In Fig. 39, we compare the peak amplitudes of the current densities using the same oval crossings as in Fig. 38. Again, both methods produce quite equal results. The number of included oval crossings is clearly smaller in the southern hemisphere. This is obviously due to the more complex structure of the

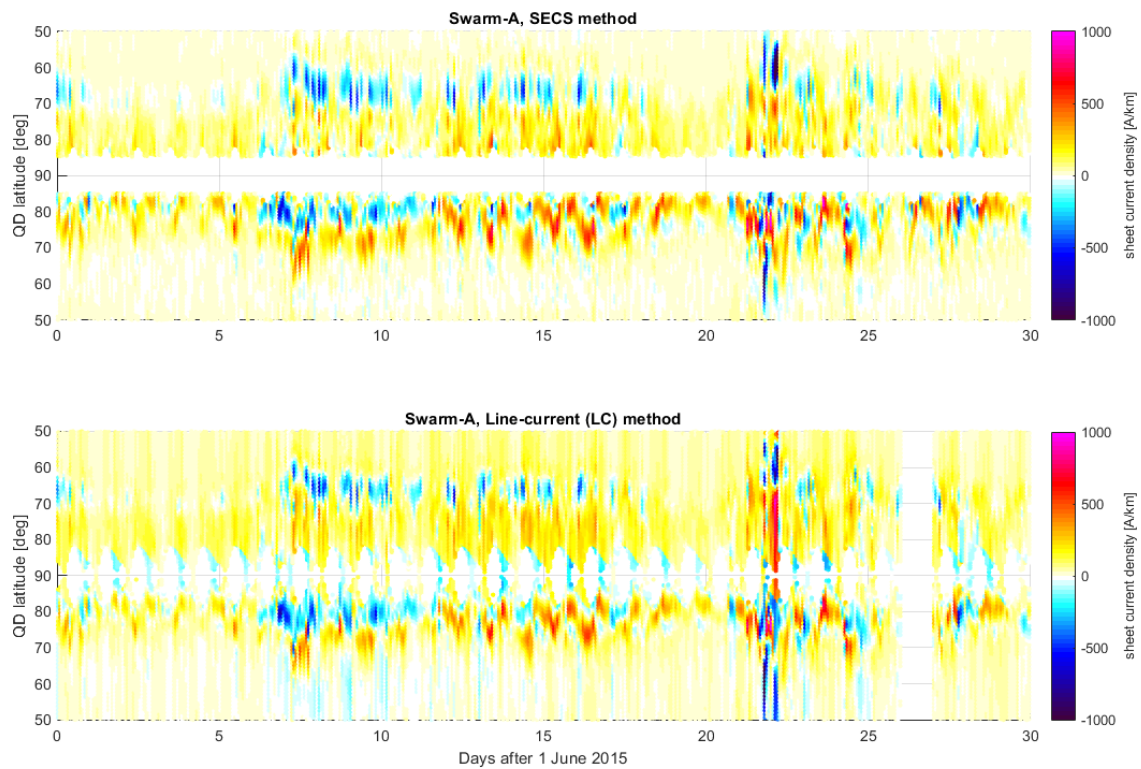


Figure 35: Time-latitude plots of Northern hemisphere sheet current density as derived from Swarm-A measurements for June 2015, using the SECS method (upper panel) and LC methods (lower panel), respectively.

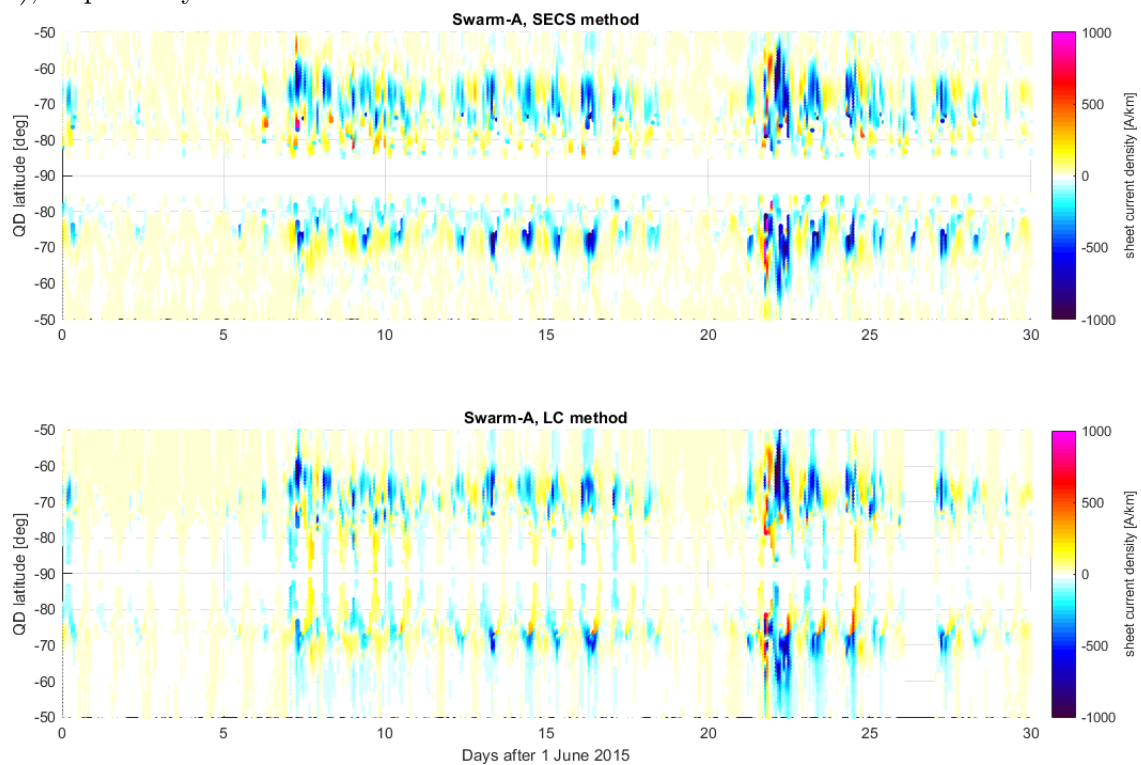


Figure 36: Similar to Fig. 35 but for the of Southern hemisphere.

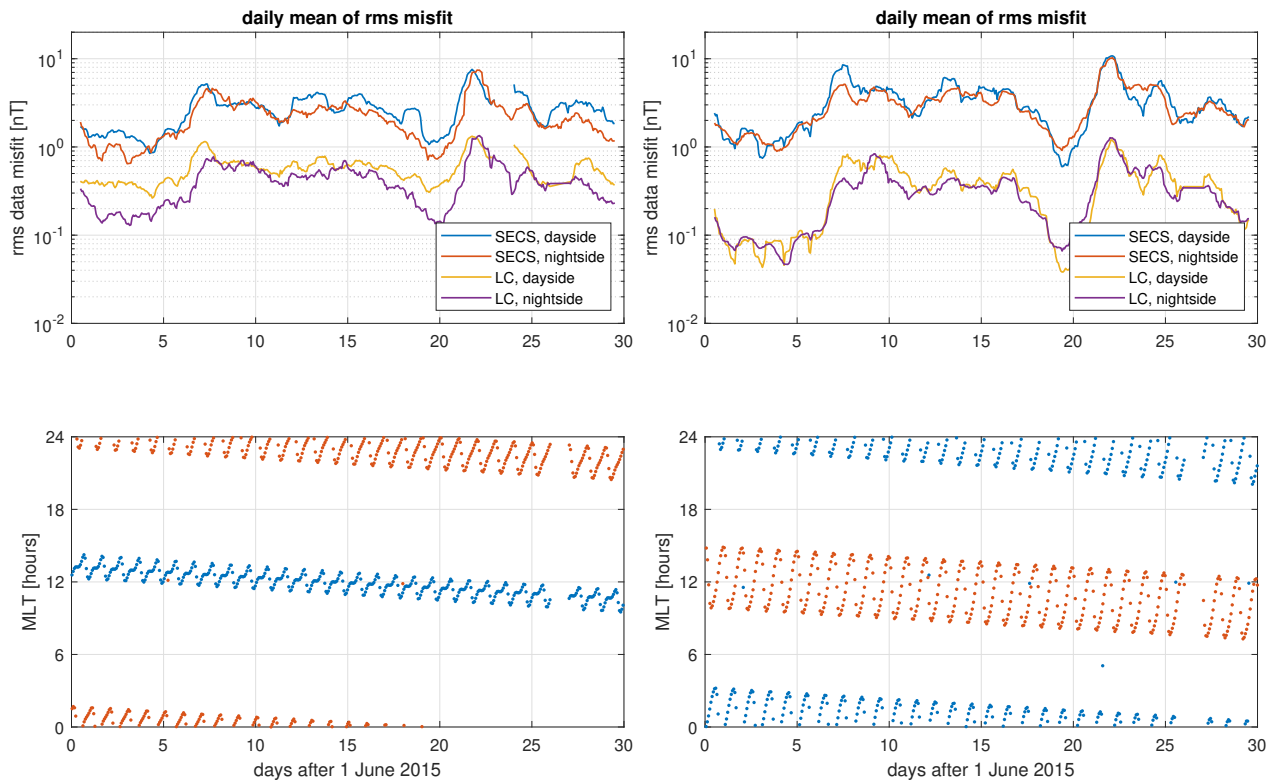


Figure 37: Top: Daily averages of rms data misfit, for the Northern (left), resp. Southern (right) hemisphere. Bottom: Magnetic local time of the satellite footprint.

main geomagnetic field there reflected to the geometry of the QD frame.

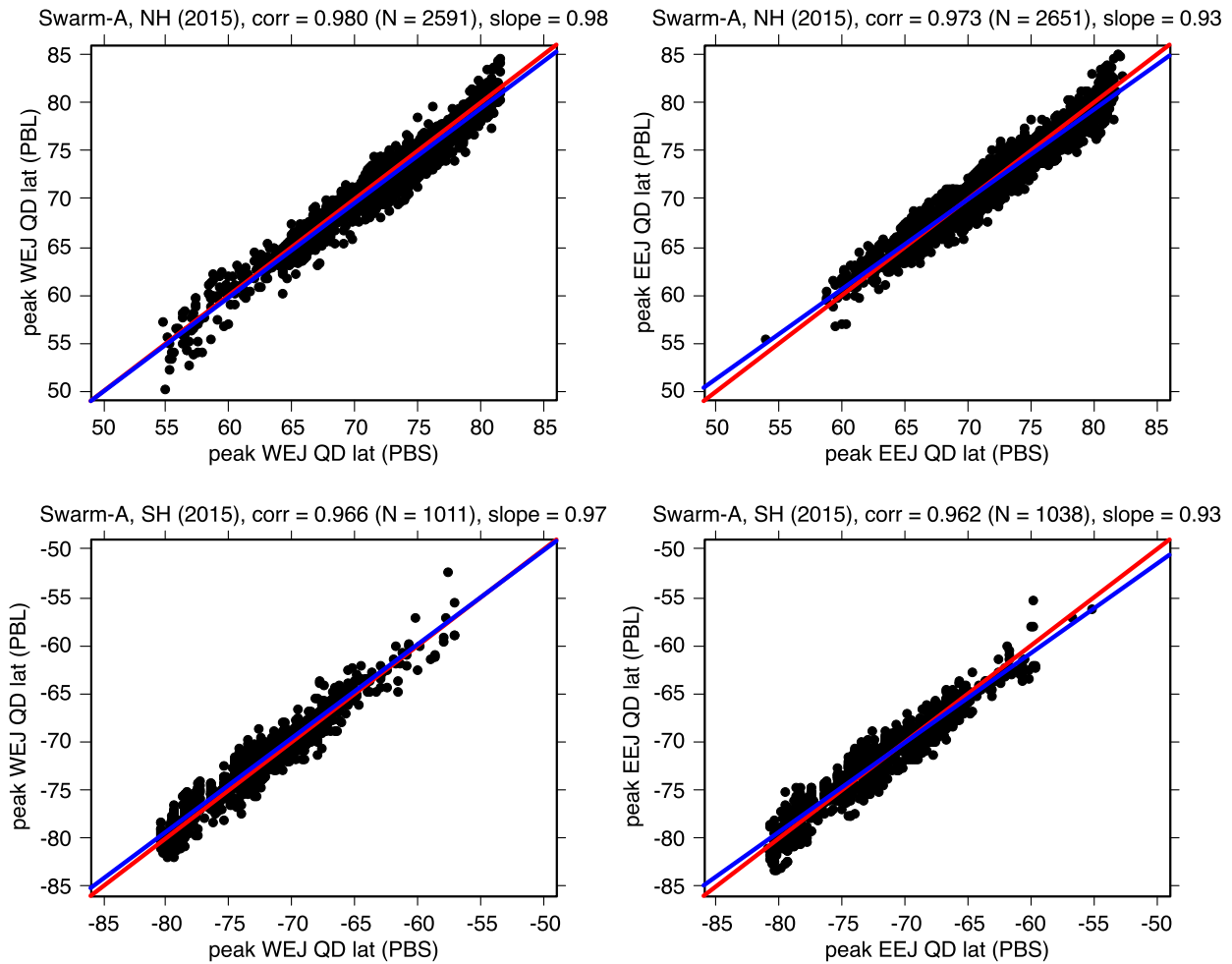


Figure 38: Quasi-dipole latitude of the peak westward (left column) and eastward (right column) current densities by the SECS and LC methods. Upper and lower rows: results for the northern and southern hemispheres, respectively. Data contains such oval crossings of Swarm-A in 2015, which have the best quality flag (all zeros) for the SECS method. The number of crossings in each plot is N . The red line has a unit slope and blue shows a fitted straight line whose slope is given in the plot title.

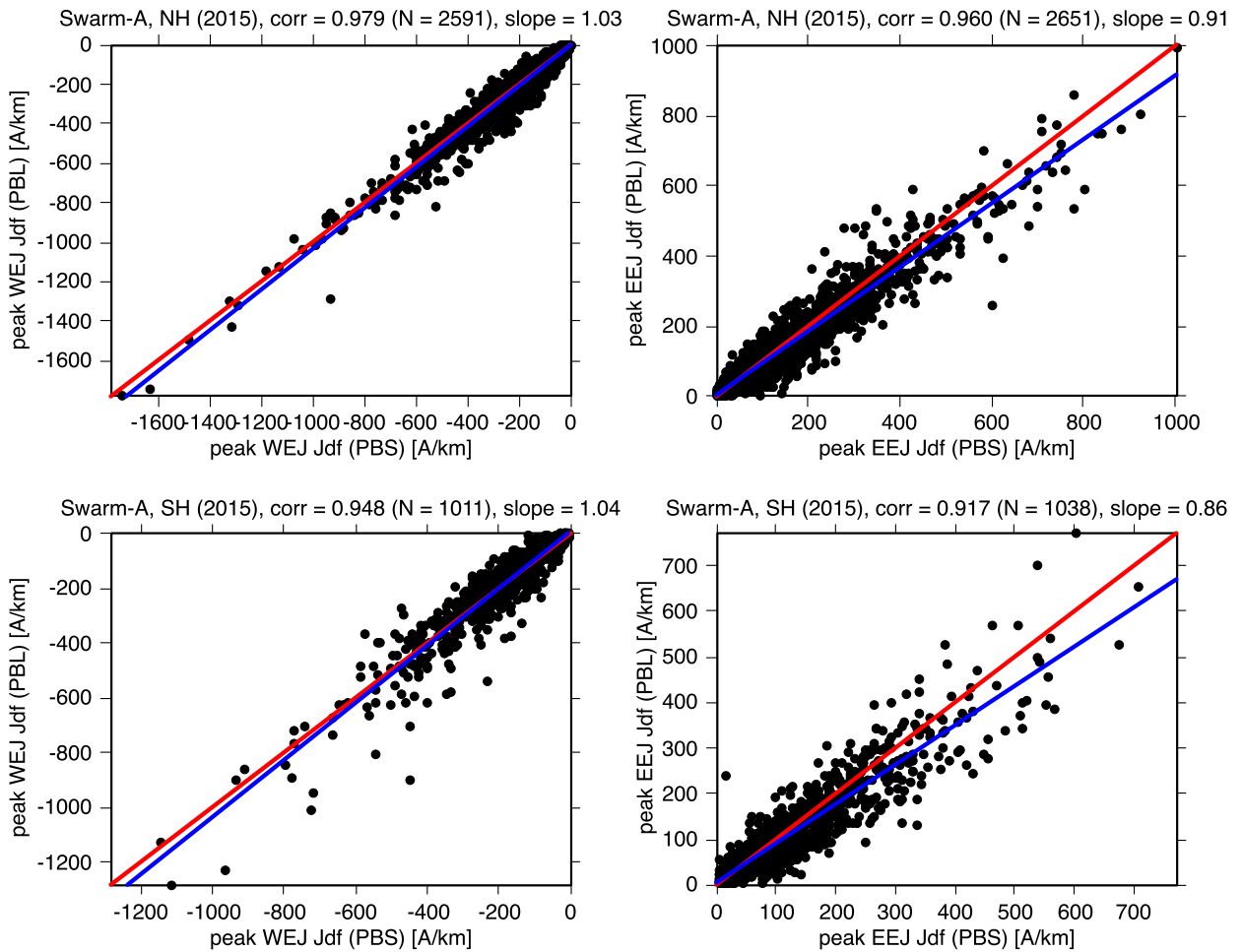


Figure 39: Peak westward (left column) and eastward (right column) current densities by the SECS and LC methods. Upper and lower rows: results for the northern and southern hemispheres, respectively. The same oval crossings are used as in Fig. 38.

4.3.2 AOB vs SECS method

The location of the auroral ovals determined by the AOB method are compared here to the locations of the westward electrojet determined by the SECS method. We assume that the boundaries of the electrojet are related to the oval boundaries based on field-aligned currents. As a test period, we used Swarm data of June 2015 (Fig. 40). The time stamp assigned to each oval of the AOB method is the mean value of the detection of the equatorward and poleward boundaries. The corresponding time stamp for the westward electrojet is the time of its peak value. We required that the difference between these time stamps is at most two minutes. There is a reasonably good correlation between the two methods. Concerning the oval width, the difference is larger as shown in Fig. 41.

4.3.3 FAC values by SECS versus L2 FAC-dual product

Figure 42 shows that in the statistical sense the radial currents from the SECS method produce similar current patterns to the L2 FAC-dual product [AD 4]. We note that the SECS results are given at the altitude of 110 km, whereas the L2 FAC-dual product results are given at the satellite altitude. Both products also show a trend of smaller median current amplitudes in the southern hemisphere compared to the northern hemisphere. However, some differences between the two products can be seen in the results near the poles, especially at the very northern (southern) edge of the analysis area in the northern (southern) hemisphere. In addition, the SECS currents in general seem to have larger amplitudes in the southern hemisphere south of the -75° line of the QD latitude. As a visual comparison, the general pattern of FACs is very similar to the results by [RD 10]

For comparison, Fig. 43 shows the horizontal current density medians. The north-south component of the current density pattern is consistent with the radial current density seen in 42, as the analysis method assumes the radial currents to close purely meridionally. The smaller amplitude of the radial currents in the southern hemisphere in Fig. 42 is seen as smaller amplitudes in the north-south component in Fig. 43. The convection electrojets are clearly seen in the eastward current. The smaller amplitude of the westward electrojet in the southern hemisphere compared to the northern hemisphere is also prominent in this representation.

Figure 44 shows the QD latitude versus magnetic local time distributions of the equatorward and poleward auroral oval boundaries, which are derived from the Level-2 field aligned current of Swarm-A. All oval crossings in March 2014 to May 2019 with the quality flag ($P_a > 0.2$ and $\sigma < 0.4$) have been taken into account. Here, P_a and σ are the slope and standard deviation of the linear fit of the S value that has been used to determine the boundaries. Results are shown for different magnetic activities, and separately for the northern and southern hemispheres. The results by Swarm-B and Swarm-C show similar distribution as that of Swarm-A, and therefore, they are not presented here. Visual comparison between Figs. 42-43 and Fig. 44 shows the expected result that the oval boundaries exist in the region where radial currents are concentrated.

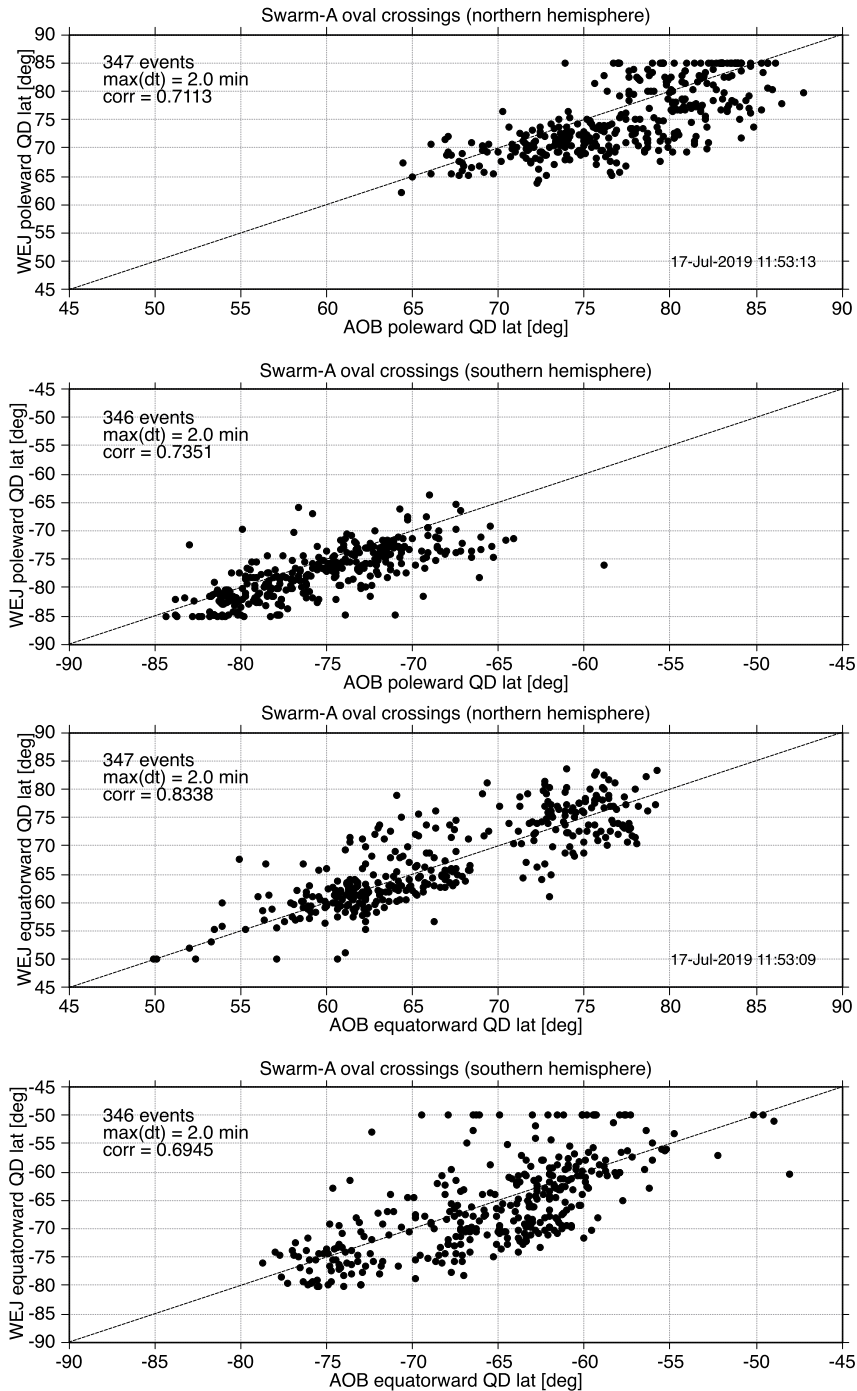


Figure 40: Poleward and equatorward boundaries of the auroral oval in June 2015 (Swarm-A). Horizontal axis: AOB refers to the method based on field-aligned currents. Vertical axis: Boundary based on the westward electrojet. A straight line with a unit slope is also shown.

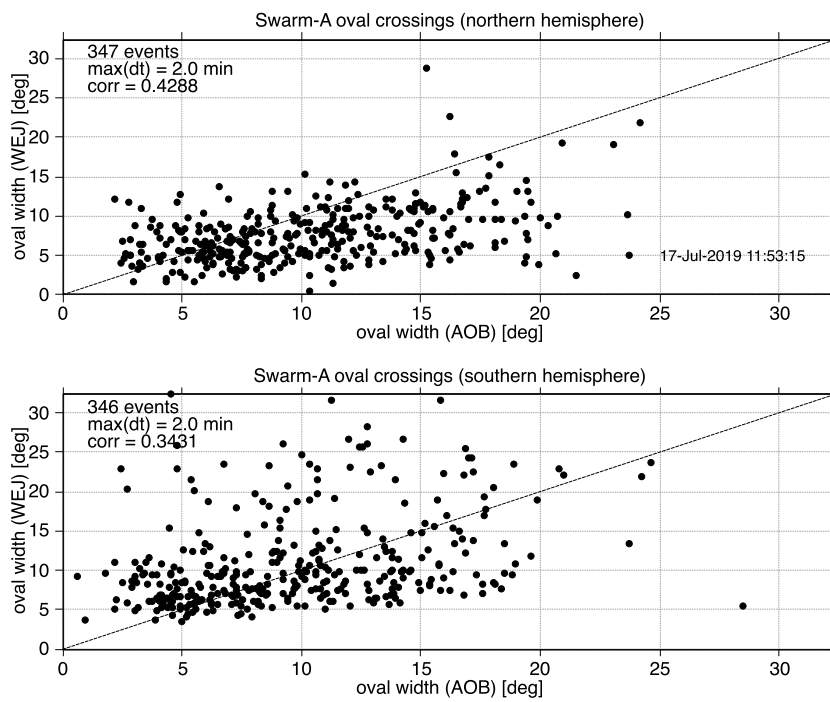


Figure 41: Auroral oval width determined from results of Fig. 40. A straight line with a unit slope is also shown.

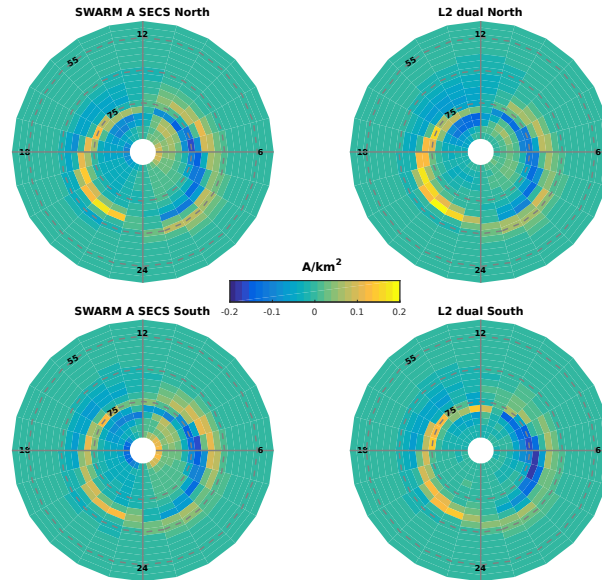


Figure 42: The median radial current densities from all oval crossings with both the SECS and L2 FAC-dual quality flags all 0, binned according to the QD latitude and magnetic local time. The data includes all oval crossings fulfilling the best quality flag requirement (all zeros) between 2014-02-27 and 2019-05-31. Top row: the northern hemisphere results for the SECS method (left) and the L2 FAC-dual product (right). Bottom row: The same for the southern hemisphere. The SECS results are given at the altitude of 110 km and the L2 FAC-dual product results at the satellite altitude.

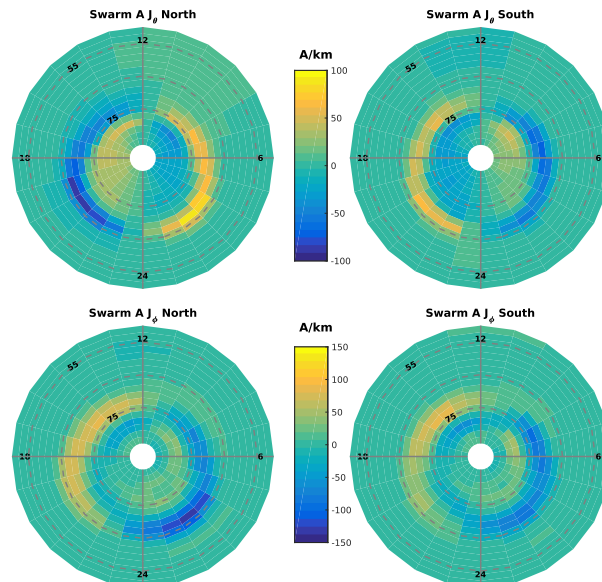


Figure 43: The median horizontal sheet current densities from the same oval crossings as in the radial current comparison. Top row: curl free currents, (J_θ , north-south, positive values towards south) for the northern hemisphere (left) and the southern hemisphere (right). Bottom row: divergence free currents (J_ϕ , west-east, positive values towards east) for the northern hemisphere (left) and the southern hemisphere (left).

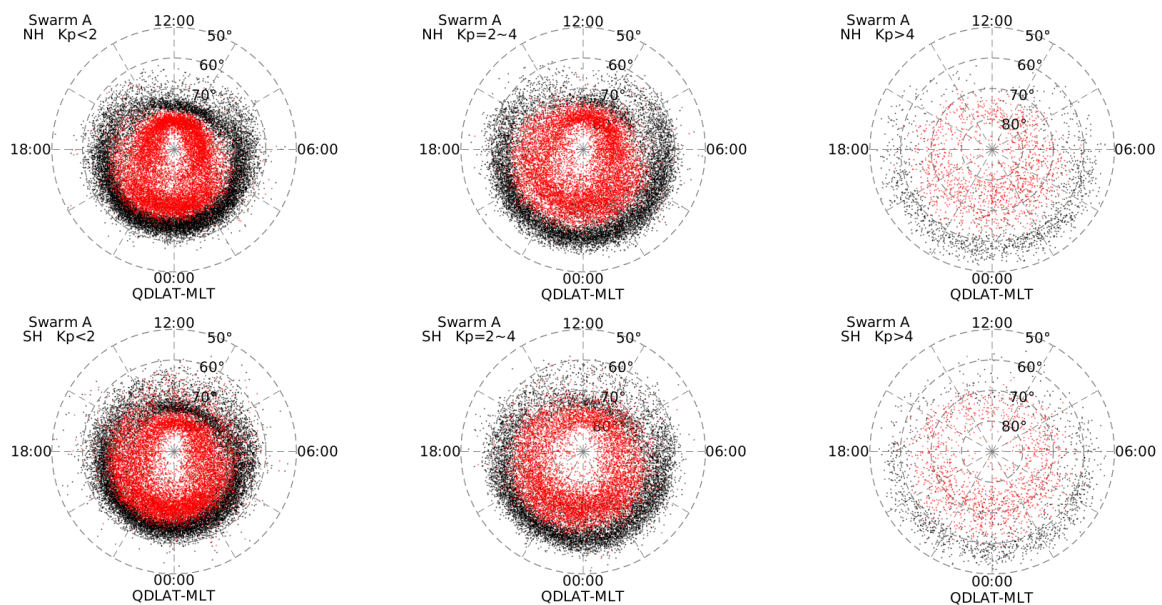


Figure 44: The equatorward (black) and poleward (red) auroral oval boundaries derived from the Level-2 field aligned current of Swarm-A. All oval crossings in March 2014 to May 2019 with the quality flag ($P_a > 0.2$ and $\sigma < 0.4$) have been taken into account. Top row: the northern hemisphere results for different magnetic activities: $K_p < 2$, $K_p = 2 - 4$, $K_p > 4$. Bottom row: The same for the southern hemisphere.

A Appendix

The Appendix contains auxiliary information of selected topics.

A.1 More details about the selection of the baseline field (SECS method)

Swarm measures the magnetic field produced by several sources. The main contribution comes from the very slowly varying fields created by currents inside Earth, and smaller effects are due to crustal anomalies close to the surface. When studying currents in space, these internal parts have to be subtracted. Space currents in turn flow both in the ionosphere close to the 100 km altitude and in the much more distant magnetosphere, and these two regions are connected by currents flowing along the geomagnetic field lines. Since the present work aims at estimating the ionospheric auroral electrojets, the magnetospheric contribution has been removed too, with an exception of comparison to the ground-based magnetic field (Sect. 4.2.2). We will now discuss in more detail how different selections of the residual field affect the modelling of electrojets.

We used data of Swarm-A of 1-29 June 2015 with three different baseline subtractions: POMME-9, CHAOS-6-Combined (VirES: CHAOS-6-Core + CHAOS-6-Static) and CHAOS-6-Combined with the subtraction of the magnetospheric contribution (VirES: CHAOS-6-MMA-Primary + CHAOS-6-MMA-Secondary). Comparison of the electrojet amplitudes is shown in Fig. A.1. POMME-9 and CHAOS-6-Combined produce quite equal estimates. Larger differences are seen when the CHAOS-6 results are compared with and without the magnetospheric contribution. Subtraction of the magnetospheric field leads to distinctly larger EEJ amplitudes than in case of subtracting only the internal geomagnetic field. However, the situation is opposite for WEJ.

When the width of the electrojet is estimated, there are large differences between POMME-9 and CHAOS-6-Combined (Fig. A.2). However, when we consider only cases when the amplitude exceeds 100 kA (by POMME-9), there is a much better correspondence. For the CHAOS-6 model with and without the magnetospheric contribution, there are systematic differences. For EEJ, there is a large group of points showing wider electrojets when the magnetospheric contribution is taken into account. For WEJ, the situation is opposite. Even for electrojets exceeding 100 kA in amplitude, there are many cases with large differences.

On the other hand, centres of the electrojet have quite a good agreement independently of the baseline model (Figs. A.3-A.4). Especially, for strong currents exceeding 100 kA there are only a few outliers. For weaker currents, there are larger differences in the southern hemisphere.

The difference between the CHAOS-6-Combined and CHAOS-6-Combined with the magnetospheric contribution can be most easily understood by looking at single current density profiles (Fig. A.5). It turns out that when the magnetospheric contribution is subtracted from Swarm measurements, the ionospheric current density is typically shifted up compared to the case with the pure CHAOS-6-Combined subtraction. This increases the eastward current and decreases the westward current. As is now intuitively clear, EEJ becomes wider and WEJ becomes narrower, respectively. The width is much more sensitive to the baseline selection than the total electrojet amplitude (cf. Figs. A.1 and A.2), and large differences occur also for strong electrojets. On the other hand, the centre of the electrojet remains quite stable independently of the baseline. Namely, a shift in the current density curve should not affect the location of the minimum and maximum. During intense events with J_{df} reaching several 100 A/km, the selection of the baseline model has obviously less effect on detecting the electrojets. Since the AEBS products prepared within this project use a fixed choice of the baseline field models, a possible future development could be an interactive service, in which the user can select the baseline models.

It is recommended that, whenever possible, estimated electrojets based on Swarm data are

checked against ground-based magnetometer recordings from the same region. The ground field is affected by the same sources as the field recorded by Swarm. A very strict approach would require that the baseline of the ground field should be determined in an equivalent way to Swarm. However, this is obviously quite an impractical condition. It is clear that the quiet time field corresponding to Earth's internal main field need to be removed. It is more complicated to estimate the magnetospheric contribution separately from the ionospheric one, and it has not been done here when comparing IMAGE and Swarm.

We must also keep in mind that the 1D assumption of the SECS method leads to unavoidable inaccuracies as demonstrated by ground-based comparisons. This cannot be helped even by the most sophisticated baseline field selection.

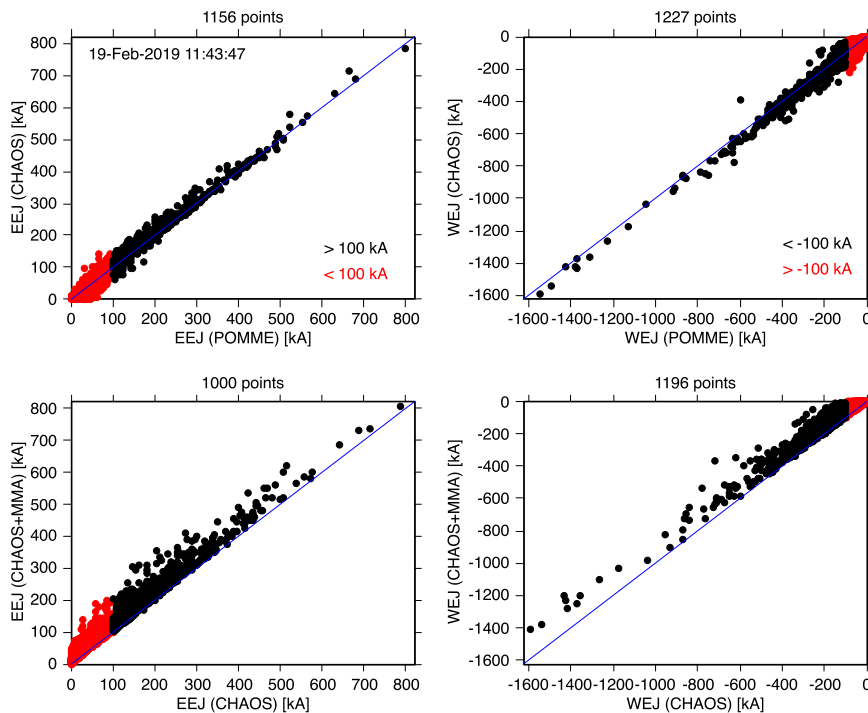


Figure A.1: Top left: amplitude of EEJ with the POMME-9 model versus CHAOS-6-Combined. Bottom left: amplitude of EEJ with CHAOS-6-Combined model versus CHAOS-6-Combined with the magnetospheric contribution. Right: similar plots for WEJ. Swarm-A data of 1-29 June 2015 is used. The blue straight line has the unit slope. Black dots show cases when the amplitude of the current corresponding to the horizontal axis exceeds 100 kA and red dots to those below 100 kA.

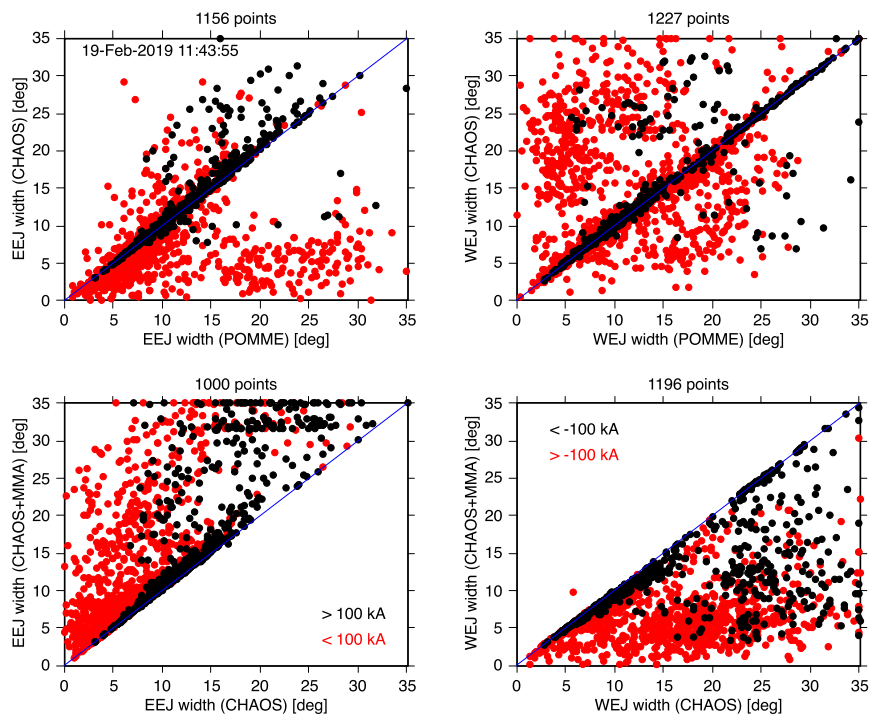


Figure A.2: Top left: width of EEJ with the POMME-9 model versus CHAOS-6-Combined. Bottom left: width of EEJ with CHAOS-6-Combined model versus CHAOS-6-Combined with the magnetospheric contribution. Right: similar plots for WEJ. Swarm-A data of 1-29 June 2015 is used. The blue straight line has the unit slope. Black dots show cases when the amplitude of the current corresponding to the horizontal axis exceeds 100 kA and red dots to those below 100 kA.

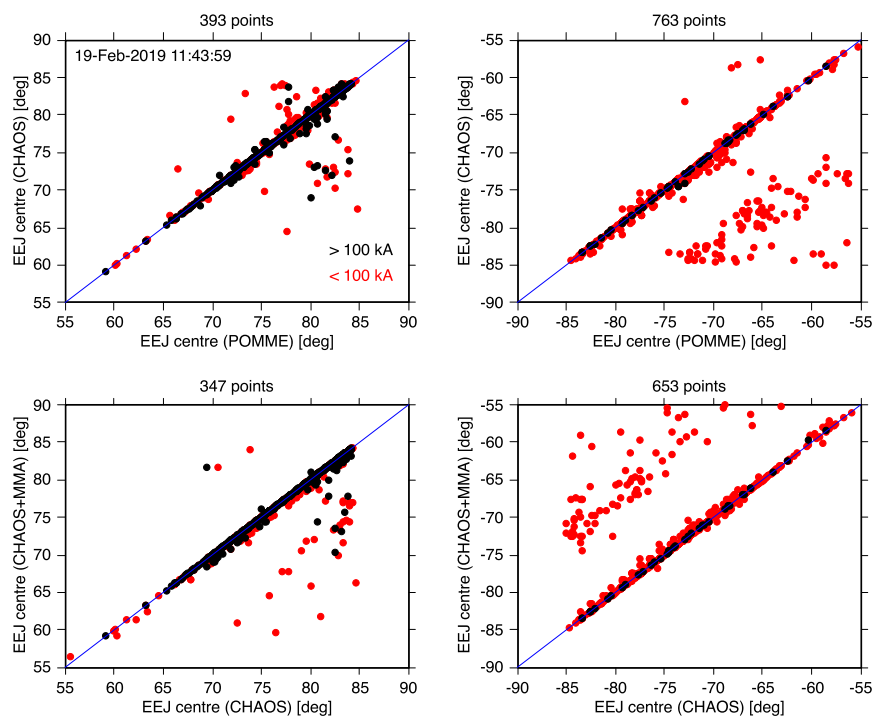


Figure A.3: Top left: centre of EEJ in the northern hemisphere with the POMME-9 model versus CHAOS-6-Combined. Bottom left: centre of EEJ in the northern hemisphere with CHAOS-6-Combined model versus CHAOS-6-Combined with the magnetospheric contribution. Right: similar plots for the southern hemisphere. Swarm-A data of 1-29 June 2015 is used. The blue straight line has the unit slope. Black dots show cases when the amplitude of the current corresponding to the horizontal axis exceeds 100 kA and red dots to those below 100 kA.

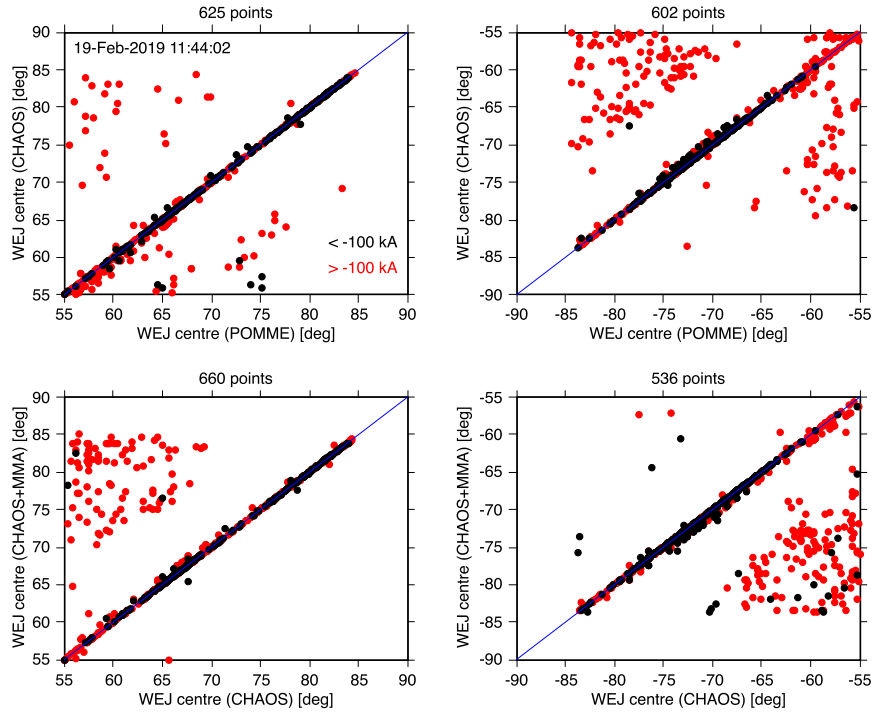


Figure A.4: As Fig. A.3 but for the westward electrojet.

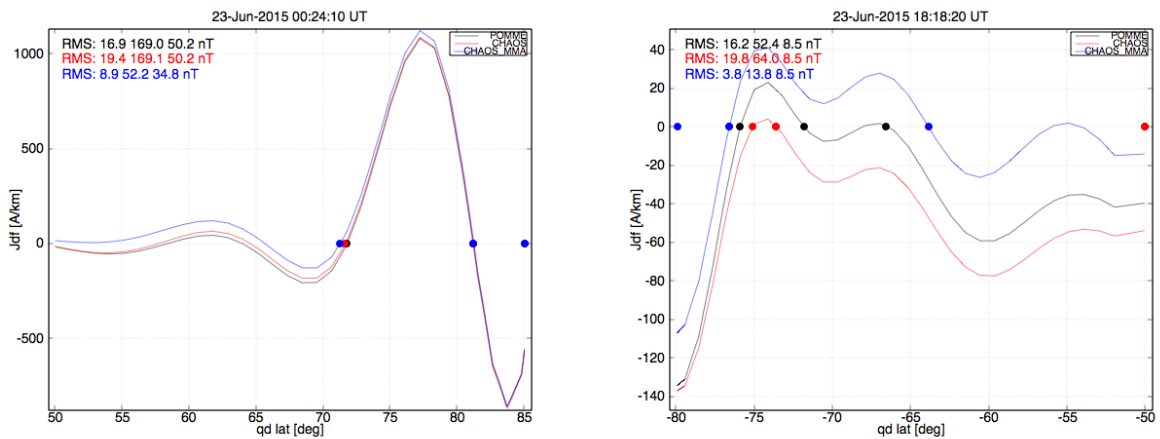


Figure A.5: Latitudinal profiles of the divergence-free ionospheric current density. Three different baseline subtractions have been applied to the measured magnetic field of Swarm-A: POMME-9 (black), CHAOS-6-Combined (red) and CHAOS-6-Combined with the CHAOS-6 magnetospheric contribution (blue). Dots indicate the boundaries of electrojets in case it has been possible to determine them.

A.2 Statistical results (SECS method)

Since Swarm-A, Swarm-B and Swarm-C give very similar results, the following examples are only based on Swarm-A. All available data are used in the period 1 Dec 2013 to 31 Dec 2018. Only crossings with the best quality flag (000000000000, see Table 1) are included. The purpose is to demonstrate that the results look reasonable. Deeper scientific analysis is left for peer-reviewed publications.

Distribution of the amplitude of the eastward and westward current in the QD frame is shown in Fig. A.6. The eastward current has a slightly smaller average amplitude than the westward one. Hemispherical differences are small for both electrojets. As a side note, we remark that the number of included oval crossings in the southern hemisphere is less than half of the number in the northern hemisphere. This is possibly due to the location of the southern QD pole that is more far away from the corresponding geographic pole than the northern QD pole. Then Swarm's (geographically) polar orbit is not so favourable for detecting ovals.

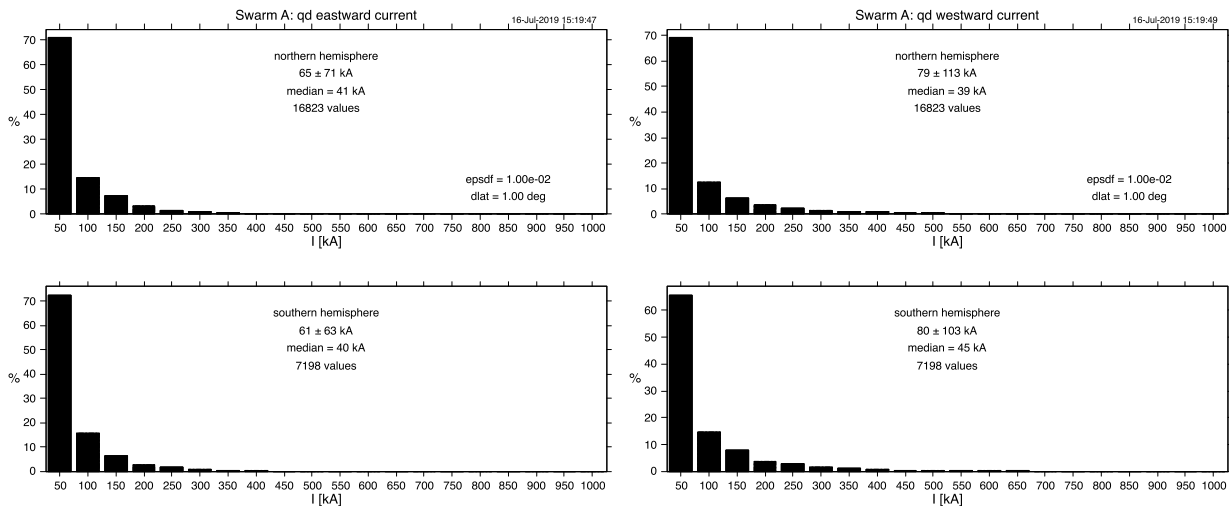


Figure A.6: Left: Distribution of the amplitude of the eastward ionospheric current in Dec 2013 to May 2019 based on Swarm-A. Upper row: northern hemisphere, lower row: southern hemisphere. Only oval crossings with the quality flag 000000000000 are included. Right: Corresponding distribution of the amplitude of westward ionospheric current. The epsilon parameter (epsdf) and the latitude step (dlat) of SECS systems are shown in the upper plots. For details concerning the parameters, see [AD 2].

Figure A.7 shows the distribution of the width of the currents. The westward current is slightly narrower than the eastward one. We note that the difference in the widths also depends on the selection of the baseline field model as discussed in Sect. A.1.

The location of the maximum ionospheric sheet current density is presented in Fig. A.8. The distributions are quite similar in both hemispheres, but the poleward peak in the distribution is more prominent in the south. The maximum around ± 73 deg is obviously related to the 'proper' electrojet, whereas the poleward maximum is related to return currents across the polar cap. The latitude axis is limited to $\pm 50 \dots \pm 85$ deg, i.e. the predefined oval range in QD coordinates. Since we use only crossings with the best quality flag, the maximum current density cannot clearly occur very close to ± 50 deg or ± 85 deg.

The number of different quality flag combinations for Swarm-A in Dec 2013 to Dec 2018 is

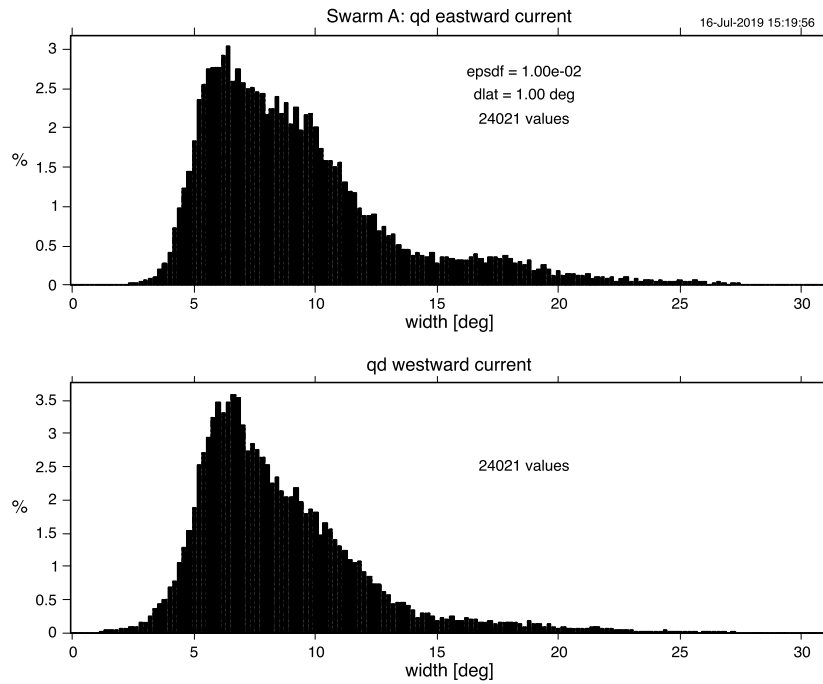


Figure A.7: Distribution of the width of ionospheric currents in Dec 2013 to Dec 2018 based on Swarm-A. Upper plot: eastward current, lower plot: westward current. Only oval crossings with the quality flag 000000000000 are included. The epsilon parameter (epsdf) and the latitude step (dlat) of SECS systems are shown in the upper plot.

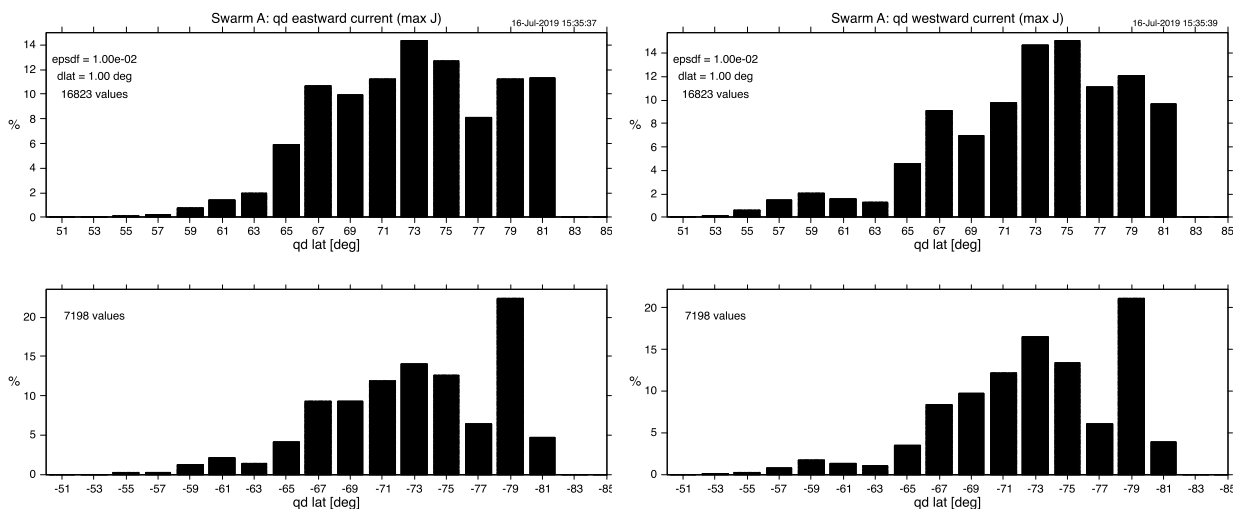


Figure A.8: Left: Distribution of the latitude of the maximum eastward ionospheric current density in Dec 2013 to Dec 2018 based on Swarm-A. Upper row: northern hemisphere, lower row: southern hemisphere. In both plots, the right end of the latitude axis is at the QD pole. Only oval crossings with the quality flag 000000000000 are included. Right: Corresponding distribution of the westward electrojet. The epsilon parameter (epsdf) and the latitude step (dlat) of SECS systems are shown in the upper plots.

Table A.1: Number of different quality flag combinations for Swarm-A in Dec 2013 to Dec 2018. Only combinations with proportion larger than 1% are shown. See Table 1 for the explanation of the flags.

flag	count	%
000000000000	24021	19.5
0000100001000	10333	8.4
0000001000000	10313	8.4
0000101001000	9235	7.5
0010000100000	8264	6.7
1000001100000	7825	6.3
0100001001000	7201	5.8
0010001100000	6884	5.6
0000100000000	5155	4.2
0010000000000	3833	3.1
0010010100000	2153	1.7
0000111001010	2063	1.7
0000010000000	2056	1.7
0000011000100	1644	1.3
0100011001110	1321	1.1
0001000010000	1212	1.0
0000010000100	1184	1.0

shown in Table A.1. There are altogether 102 combinations, but the table lists only those whose proportion is at least 1%. The most ideal case (000000000000) occurs in 19.5% of all oval crossings (for reference, both Swarm-B and Swarm-C reach 19.8% and 19.6% within the same period). In the second most common case (0000100001000), the poleward EEJ boundary occurs at the edge of the predefined oval latitude range, or at the edge of the available latitude range. Additionally, the current density is there more than 20% of the peak value. In the third most common case (0000001000000), Swarm does not cross the full predefined oval range, but the electrojets are still properly detected.

It is also important notice that even the best case (all zeros) does not guarantee that there are proper electrojets. This is demonstrated when comparing results to ground-based data in Sect. 4.2.2.

A.3 Empirical AOBFAC model vs DMSP AOB product

Related to Sect. 4.2.5, we compare here the empirical AOBFAC model with the DMSP AOB product. Figure A.9 shows results for 2014. The ΔMLAT is defined as the model prediction minus the DMSP AOB product. The top panel shows the correlation between (left) equatorward and (right) poleward auroral boundaries around 19 MLT; the empirical model underestimates the equatorward boundary by about 5° , while it overestimates the poleward boundary by about 2. The bottom panels show the median value as well as rms of ΔMLAT for all available MLT. For the equatorward boundary, the median values of ΔMLAT are within $\pm 5^\circ$, and they show anti-phase trend in the dawn and dusk sectors for both hemispheres. Similar anti-phase trend during dawn and dusk hours is also found for the poleward boundary in the southern hemisphere, but the empirical model generally overestimates the poleward boundary in the northern hemisphere.

As AOB product derived from DMSP satellite is based on the particle precipitation measurements, while our empirical model is based on the AOB product derived from FAC signatures of CHAMP and Swarm satellites, the difference between them may imply that there are systematic differences, e.g., dependence on MLT, between the particle precipitation and FACs. Further investigation is needed for addressing this point.

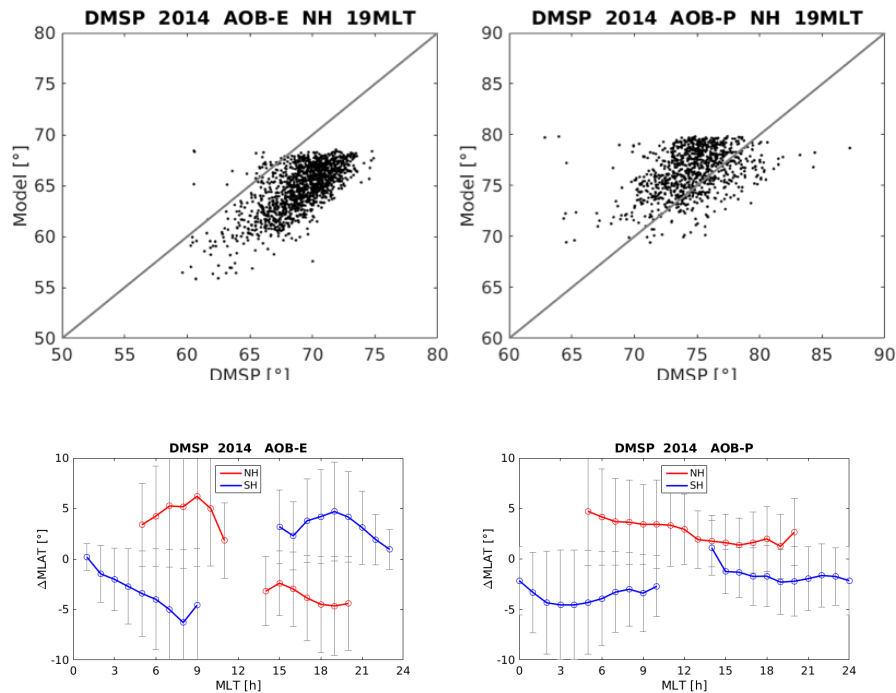


Figure A.9: Correlation (top) and difference (bottom) between the empirical model (AOBFAC) predictions and the DMSP AOB product for equatorward (left) and poleward (right) boundaries. DMSP data of the one-year period of 2014 are used here.

A.4 Remarks of quality flags

Ionospheric currents in the polar cap are not suppressed in the LPL data products, as is the case for the LPS products. Thus the poleward boundaries of the auroral electrojets are not as well defined in LPL latitude profiles as in LPS: detected boundaries will more often occur at the edge of the analysis area in PBL products compared to PBS. Hence the occurrence of PBL Flag = 0 values (indicating well-defined boundaries) is much lower than for PBS (see Fig. A.10). The presence of polar cap currents in the LPL latitude profiles results in more poleward boundaries detected at the edge of the analysis area.

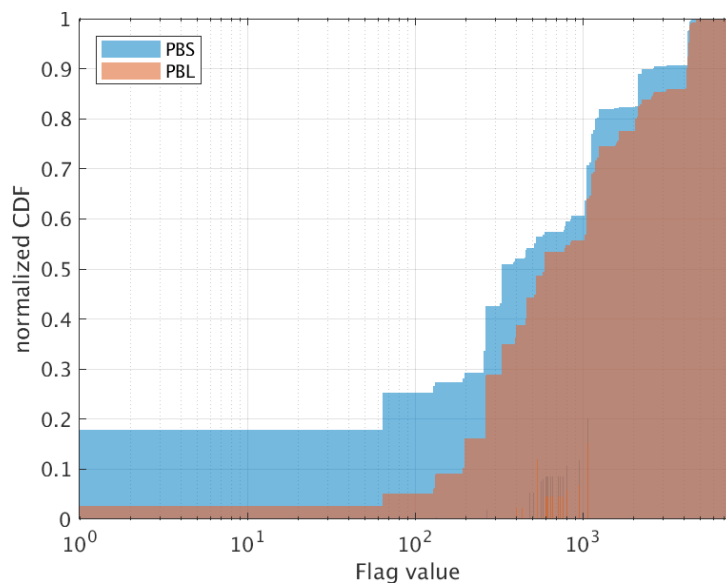


Figure A.10: Comparison of PBS and PBL flag values for the year 2014. 17.8% of the PBS data have Flag = 0 whereas only 2.7% of the PBL data have Flag = 0.

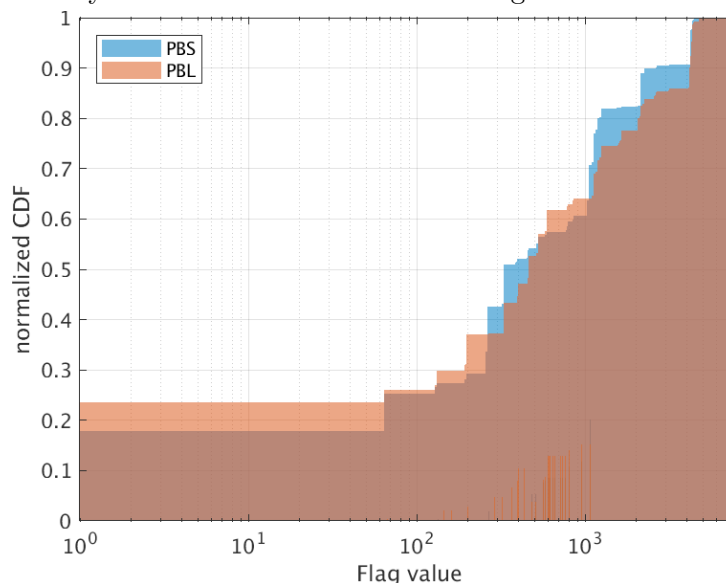


Figure A.11: Comparison of PBS and PBL flag values for the year 2014. 17.8% of the PBS data have Flag = 0, whereas approximately the same amount (27%) of the PBL data have similar Flags values when ignoring flags 9, 11, 9+4 and 11+6.

There are flags related to the occurrence of the poleward electrojet boundary at the edge of the analysis area. Ignoring these flags (9, 11, 9+4 and 11+6) by setting these to binary values = 0 results in a distribution of PBL flags (see Fig. A.11) that is closer to that of the PBS flags.

This is confirmed by the statistics of bit occurrence in PBL and PBS Flag values (see Fig. A.12). In general, more bits occur in PBL Flag values because the auroral electrojet boundaries are not as well defined in LPL latitude profiles as in LPS latitude profiles, and especially bits 4, 6, 9 and 11 occurs more often due to the presents of polar currents in LPL latitude profiles.

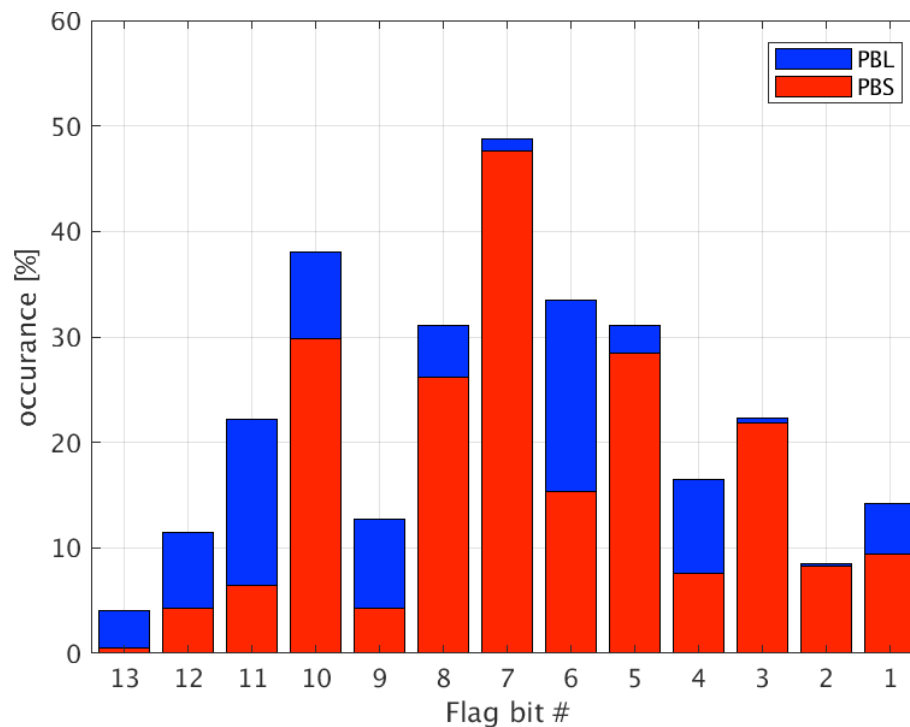


Figure A.12: Statistics of bit occurrence in PBL and PBS Flag values. More bits occur in PBL Flag values because the auroral electrojet boundaries are not as well defined in LPL latitude profiles as in PBS latitude profiles due to polar cap currents. Especially bits 4, 6, 9 and 11 occur more often due to the presents of polar cap currents in LPL latitude profiles.